J. Fluid Mech. (1986), *vol.* 165, *pp.* 163–199
Printed in Great Britain

A theoretical and experimental study of wall turbulence

By A. E. PERRY, S. HENBEST AND M. S. CHONG
University of Melbourne, Department of Mechanical Engineering, Parkville, Victoria 3052, Australia

(Received 6 November 1984 and in revised form 5 October 1985)

In this paper the dimensional-analysis approach to wall turbulence of Perry & Abell (1977) has been extended in a number of directions. Further recent developments of the attached-eddy hypothesis of Townsend (1976) and the model of Perry & Chong (1982) are given, for example, the incorporation of a Kolmogoroff (1941) spectral region. These previous analyses were applicable only to the 'wall region' and are extended here to include the whole turbulent region of the flow. The dimensional-analysis approach and the detailed physical modelling are consistent with each other and with new experimental data presented here.

1. Introduction

The study and description of wall-bounded shear flows has been an active and challenging field for most of this century. By the end of the 1930s various phenomenological theories had been proposed which were aimed mainly towards describing the mean flow. These theories were unconvincing and little or no serious attempt was made to extend them to include the fluctuating quantities. Izakson (1937) and Millikan (1939) then developed a dimensional-analysis approach for the mean flow, based on the existence of a 'region of overlap' in which two mean-flow similarity laws are simultaneously valid, to establish the logarithmic law of the wall and laws of skin friction in pipes, ducts and boundary layers. This approach is also based on the study of how experimental data collapse when plotted with different sets of scaling coordinates. These coordinates are determined from physical considerations and dimensional analysis. Such an approach has little regard for the detailed physical processes involved and relies only on physical assumptions of a general nature. However, if successful, it establishes a functional framework for the correlation of experimental data and further detailed physical modelling must be consistent with this framework.

The application of this approach to the fluctuating quantities has not met with the same success as it has with the mean flow, partly because of the difficulties involved in obtaining accurate experimental data. Perry & Abell (1975) applied the approach to their broadband streamwise-turbulence data obtained in smooth-walled, fully turbulent pipe flow. They postulated an 'inner-flow' and an 'outer-flow' scaling law for the $\overline{u_1^2}/U_\tau^2$ distribution (where $\overline{u_1^2}$ is the mean square of the fluctuating streamwise velocity and U_τ is the mean wall shear velocity) and deduced that $\overline{u_1^2}/U_\tau^2$ is a universal constant in the region of overlap, where both laws are simultaneously valid. This region coincides with that portion of the boundary layer in which the mean-flow logarithmic law of the wall is valid and the Reynolds shear stress can be considered to be constant, and will be referred to as the turbulent wall region.

In the light of further work Perry & Abell (1977) revised their ideas. By utilizing their streamwise spectral data (measured in the turbulent wall region) and the physics of Townsend's (1976) attached-eddy hypothesis, they proposed certain spectral-similarity laws, deduced their analytical form in the spectral regions of overlap and from these laws predicted the distribution of $\overline{u_1^2}/U_\tau^2$ in the turbulent wall region.

A physical model consistent with the above findings was attempted by Perry & Chong (1982), hereinafter referred to as PC. This model was based on the flow-visualization results of Head & Bandyopadhyay (1981) and the attached-eddy hypothesis of Townsend (1976). They proposed that a wall shear layer is made up of a forest of attached hairpin, Λ-shaped or horseshoe vortices inclined in the downstream direction at approximately 45° to the wall. Head & Bandyopadhyay point out that the eddies maintain this angle for some distance as they are convected downstream. Recent work by Smith (1984), Acarlar & Smith (1984), Moin & Kim (1985) and Kim (1985) further supports the existence of hairpin vortices in wall turbulence. For simplicity, PC confined their attention to Λ-shaped vortices. Beginning with an isolated Λ-vortex they showed that because of its image in the wall the vortex undergoes a stretching process in which the vortex height h increases approximately uniformly with time and the distance λ between the 'legs' of the vortex at the wall decreases such that the product λh remains constant (a plane-strain-like motion in the plane of the vortex). They also showed that viscous diffusion ultimately dominates the stretching process and proposed that when the legs of the Λ-vortex eventually come together the vortex dies by vorticity cancellation. A random array of Λ-shaped vortices, all at different stages of stretching but with the same circulation, was called a 'hierarchy'. They found that, in order to obtain a logarithmic mean-velocity distribution, a region of constant Reynolds shear stress and the correct u_1 spectral behaviour in the turbulent wall region, it is necessary to assume that a range of scales of geometrically similar hierarchies exist. The simplest assumption is that all hierarchies have the same velocity scale ($\sim U_\tau$)† and that their lengthscale δ varies. The probability density function (p.d.f.) of hierarchy scale δ follows a geometric progression for a discrete distribution and an inverse power law if a continuous distribution is assumed. The lengthscale of the hierarchies vary from the smallest scale δ_1, which is assumed to be proportional to the Kline *et al.* (1967) scaling (i.e. $\delta_1 \sim \nu/U_\tau$, where ν is the kinematic viscosity), to the largest scale Δ_E, which is assumed to scale with the shear-layer thickness. How these hierarchies form is a mystery but one possible explanation suggested by PC is vortex pairing: the eddies in the smallest hierarchy form from a roll-up of viscous-sublayer material and, although most of the eddies in this hierarchy die, some manage to pair to form eddies belonging to the next hierarchy; most of the eddies in the next hierarchy die but some manage to pair to form eddies belonging to the next hierarchy and so on. PC assumed a discrete p.d.f. of hierarchy lengthscales that doubled from one hierarchy to the next, and suggested that the effect of 'jitter' or randomness about each discrete hierarchy scale gives a continuous inverse-power-law p.d.f. Their proposals are consistent with those of Townsend (1976), who effectively replaced each hierarchy with a group of identical 'representative eddies' and assumed an inverse-power-law p.d.f. for the representative eddy lengthscales in his broadband turbulence-intensity analysis. Acarlar & Smith (1984) have shown that the speculated pairing process does in fact occur, at least for hairpin-type vortices formed in the region behind rivet heads. Whether such pairing occurs in turbulent boundary layers is an open question.

PC's model was successful in linking the mean-flow similarity laws with the

† Throughout this paper $\sim$ means 'proportional to' or 'scales with'.

streamwise turbulence spectra and the broadband turbulence-intensity distributions in the turbulent wall region. However, no account was taken of the possibility that the attached eddies are surrounded by fine-scale isotropic eddies, which gives rise to a Kolmogoroff (1941) spectral region, which includes an inertial subrange if the Reynolds number of the flow is sufficiently large. Unfortunately, PC used the data of Perry & Abell (1977) in which a Kolmogoroff region with an inertial subrange was not obvious. Here we present strong experimental support for the existence of such a region and attempt to explain its existence and how it fits in with PC's model. We begin in §2 by extending the spectral analysis of Perry & Abell (1977) to three dimensions. In §3, the model of PC is improved and extended to include the 'wake' region (i.e. the region beyond the turbulent wall region). The analysis establishes a link between low-wavenumber spectra of motions parallel to the wall in the turbulent wall region and the mean-flow deviation from the logarithmic law of the wall in the wake region. The outcome is a model which the authors consider to be applicable to the whole turbulent region in zero-pressure-gradient boundary layers. With slight modifications it should also be applicable in pipe and duct flow. Experimental spectral and turbulence data obtained in smooth-walled fully developed pipe flow are presented in §4 and these give strong support to the model of wall turbulence presented here.

2. A dimensional-analysis approach to wall turbulence

We will consider here some examples of turbulent wall-shear flow over a smooth surface. Much of the analysis is applicable to a slowly developing turbulent boundary layer on a flat wall with zero streamwise pressure gradient, to fully developed turbulent flow in a circular pipe and to flow in a high-aspect-ratio rectangular duct. Let Δ_E be a characteristic lengthscale of the outer part of the shear layer. This would scale with the boundary-layer thickness, pipe radius or duct half-width. Let the symbol $\overline{U_{1E}}$ represent the velocity at the edge of the boundary layer, the mean velocity at the pipe axis or at the plane of symmetry of the duct. Let x be the streamwise coordinate, y the cross-stream distance, z the distance normal to the wall and let the corresponding velocity components be U_1, U_2 and U_3. Overbars will denote mean values and lower-case letters will denote fluctuating quantities.

It is well known that in a region close to the wall, the mean flow follows Prandtl's law of the wall

$$\frac{\overline{U_1}}{U_\tau} = f_1\left[\frac{zU_\tau}{\nu}\right]. \tag{1}$$

The function f_1 is universal and independent of the large-scale flow geometry (i.e. independent of whether we have boundary layer, pipe or duct flow). For the fully turbulent region (i.e. the region of flow beyond the buffer zone) the mean flow follows the velocity-defect law

$$\frac{\overline{U_{1E}} - \overline{U_1}}{U_\tau} = f_2\left[\frac{z}{\Delta_E}\right]. \tag{2}$$

The function f_2 is universal only for a given large-scale flow geometry. Millikan (1938) assumed 'that there is possibly a small but finite region near the wall in which both (1) and (2) are valid ...' and deduced that within the region of overlap

$$\frac{\overline{U_1}}{U_\tau} = \frac{1}{\kappa}\ln\left[\frac{zU_\tau}{\nu}\right] + A, \tag{3}$$

$$\frac{\overline{U_{1E}} - \overline{U_1}}{U_\tau} = -\frac{1}{\kappa}\ln\left[\frac{z}{\Delta_E}\right] + B, \tag{4}$$

by equating the velocity gradients given by (1) and (2). Here κ and A are universal constants and the constant B is dependent on the large-scale flow geometry. Constants dependent on the large-scale flow geometry will henceforth be referred to as 'large-scale characteristic constants'.

It will be assumed that the mean-flow vorticity and the energy-containing turbulent motions, which include the Reynolds-shear-stress motions, are caused by anisotropic coherent eddies attached to the wall in the sense of Townsend (1976, pp. 152–3) and PC. Many definitions for the terms coherent structure or coherent eddy exist (see e.g. Hussain 1982). The present authors regard coherent attached eddies as having similar recognizable patterns with a fixed angle of inclination relative to the wall (i.e. θ = constant as shown in figure 1) that recur throughout the flow with a range of lengthscales. These coherent eddies are assumed to be surrounded by a fluid which contains fine-scale detached eddies. The motions in this surrounding fluid are assumed to be statistically isotropic and statistically irrotational. These fine-scale eddies contribute little to the broadband turbulence intensities and make no contribution to the Reynolds shear stress but are responsible for most of the energy dissipation in the flow. They are possibly the remainder of what were once attached eddies that have been stretched, distorted and convected away from the near-wall region by the more 'active' attached eddies, and are therefore the 'debris of dead-eddy material' (see PC regarding eddy death). Many of the above physical assumptions are not essential for the following dimensional arguments but are consistent with it and will be used in a more detailed physical argument presented in §3.

The following analysis is applicable only to flow in the turbulent wall region (i.e. $\nu/U_\tau \ll z \ll \Delta_E$). Figure 1 shows three different scales of attached eddies together with the instantaneous streamline patterns that they generate relative to an observer moving with the fluid in the far field of the eddy. These are identical with the three-dimensional Λ-shaped vortices of PC (other eddy geometries are considered later). Since we are considering the flow beyond the thin viscous sublayer, we will assume that the flow is inviscid with finite slip at the boundary. Also shown in figure 1 is a probe situated at a distance z from the wall. It is not too difficult to see that an eddy of scale $\delta_A = O(\Delta_E)$ will contribute to u_1 and u_2 at the probe location and these contributions will be invariant with z for $z \ll \Delta_E$. This invariance of u_1 and of u_2 with z is meant in the sense that, if we Taylor-series expand u_1 or u_2 with respect to z about $z = 0$ for an eddy of scale δ, then, for $z \ll \delta$, the zeroth-order term will dominate over the higher-order terms; while for u_3 the first-order term will dominate. It is clear that an eddy of scale δ_A will contribute little to u_3. An eddy of scale $\delta_B = O(z)$ will contribute strongly to u_1, u_2 and u_3 and these motions will depend on z. Eddies of scale $\delta_C \ll z$ will not contribute to any motions at z because of the very small far-field effect above the eddy (see the Biot–Savart-law calculations of PC). Thus, only eddies of scale $\delta = O(z)$ contribute to u_3 motions and all eddies of scale $\delta \geqslant O(z)$ contribute to u_1 and u_2 motions at z.

Let $\Phi_{ij}(k_1)$ be the cross-power spectral density per unit streamwise wavenumber k_1 for velocity fluctuations u_i and u_j and let this be normalized such that

$$\int_0^\infty \Phi_{ij}(k_1)\,\mathrm{d}k_1 = \overline{u_i u_j}, \tag{5}$$

where i and j may equal 1, 2 or 3, and repeated indices do not denote a summation.

Let us consider the distribution of the u_1 power-spectral density, $\Phi_{11}(k_1)$, in the turbulent wall region and only that range of wavenumbers in which motions are not dependent explicitly on viscosity. This would cover most of the energy-containing

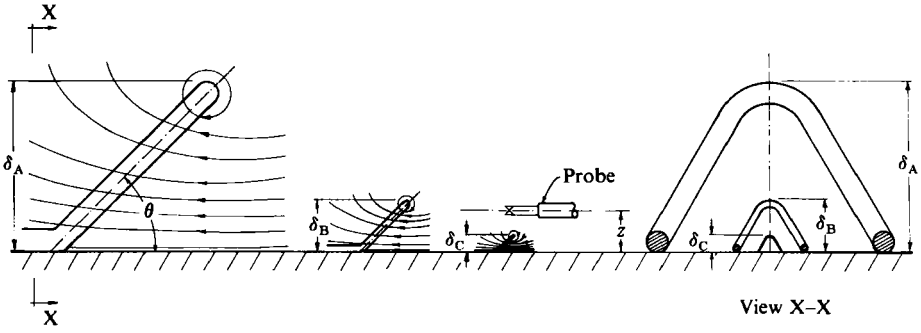

FIGURE 1. A sketch of three attached eddies of varying scales together with the instantaneous streamline pattern generated by each.

region of the spectrum since the viscosity-dependent motions would occur only at very high wavenumbers. Therefore in the energy-containing region the only variables involved are U_τ, k_1, z and Δ_E (this is in accordance with Townsend's 1976 Reynolds-number-similarity hypothesis). At $z \ll \Delta_E$, eddies of scale $\delta = O(\Delta_E)$ will contribute only to the low-wavenumber motions, so at these wavenumbers we would expect an 'outer-flow' scaling law of the form

$$\frac{\Phi_{11}(k_1 \Delta_E)}{U_\tau^2} = g_1(k_1 \Delta_E) = \frac{\Phi_{11}(k_1)}{\Delta_E U_\tau^2}, \tag{6}$$

which from earlier discussions is known to be invariant with z for $z \ll \Delta_E$. Here $\Phi_{11}(k_1 \Delta_E)$ is the power-spectral density per unit non-dimensional wavenumber $k_1 \Delta_E$. From now on the argument of a spectral function will denote the unit quantity over which the energy density is measured. Eddies of scale $\delta = O(z)$ will contribute to motions at moderate to high wavenumbers, so at these wavenumbers we would expect an 'inner-flow' scaling law of the form

$$\frac{\Phi_{11}(k_1 z)}{U_\tau^2} = g_2(k_1 z) = \frac{\Phi_{11}(k_1)}{z U_\tau^2}. \tag{7}$$

Δ_E is not involved in (7) since eddies of that scale make no contribution to this wavenumber range provided that $z \ll \Delta_E$.

Let us now consider the very-high-wavenumber viscosity-dependent motions. We would expect these motions to be locally isotropic and the u_1 spectra to follow the classical Kolmogoroff (1941) viscosity-dependent scaling law

$$\frac{\Phi_{11}(k_1 \eta)}{v^2} = g_3(k_1 \eta) = \frac{\Phi_{11}(k_1)}{\eta v^2}, \tag{8}$$

where $\eta = (\nu^3/\epsilon)^{\frac{1}{4}}$ and $v = (\nu\epsilon)^{\frac{1}{4}}$. The quantities η and v are the Kolmogoroff length and velocity scales respectively, and these depend only on the turbulent-energy dissipation ϵ and the kinematic viscosity ν. Following Townsend (1961, 1976), a reasonable assumption concerning the turbulent wall region is that turbulent energy production p and dissipation are approximately in balance,† i.e.

$$p = -\overline{u_1 u_3}\frac{\partial \overline{U_1}}{\partial z} = \epsilon. \tag{9}$$

† This contradicts the Townsend (1976) attached-eddy hypothesis. It is simple to show for flow consisting of attached eddies alone that $p/\epsilon \sim z_+$ in the turbulent wall region. The remainder of the dissipation is carried by fine-scale detached eddies surrounding the attached eddies.

In this region, $-\overline{u_1 u_3} = U_\tau^2$ and $\partial \overline{U_1}/\partial z$ is obtained using (3). From these relationships it can be shown that

$$v = \left[\frac{\nu U_\tau^3}{\kappa z}\right]^{\frac{1}{4}} \tag{10a}$$

and

$$\eta = \left[\frac{\nu^3 \kappa z}{U_\tau^3}\right]^{\frac{1}{4}}. \tag{10b}$$

Figure 2 (*a*) summarizes the various u_1 spectral regions given by (6), (7) and (8) over the range of wavenumber k_1. Two regions of overlap are anticipated, shown as 'overlap region I' and 'overlap region II'. In region of overlap I, (6) and (7) are simultaneously valid, i.e. $\Phi_{11}(k_1) = zU_\tau^2 g_2(k_1 z) = \Delta_E U_\tau^2 g_1(k_1 \Delta_E)$ and therefore $g_1(k_1 \Delta_E)/g_2(k_1 z) = z/\Delta_E$. Hence g_1 and g_2 must be of inverse-power-law form as given below:

$$\frac{\Phi_{11}(k_1 z)}{U_\tau^2} = \frac{A_1}{k_1 z} = g_2(k_1 z) \tag{11a}$$

or

$$\frac{\Phi_{11}(k_1 \Delta_E)}{U_\tau^2} = \frac{A_1}{k_1 \Delta_E} = g_1(k_1 \Delta_E), \tag{11b}$$

where A_1 is a universal constant. In region of overlap II, (7) and (8) are simultaneously valid. Substituting (10*a*) and (10*b*) into (8) and comparing this equation with (7) shows that ν is not explicitly involved. The only functional form that will permit this is

$$\frac{\Phi_{11}(k_1 \eta)}{v^2} = \frac{K_0}{(k_1 \eta)^{\frac{5}{3}}} = g_3(k_1 \eta) \tag{12a}$$

or

$$\frac{\Phi_{11}(k_1 z)}{U_\tau^2} = \frac{1}{\kappa^{\frac{2}{3}}} \frac{K_0}{(k_1 z)^{\frac{5}{3}}} = g_2(k_1 z), \tag{12b}$$

where K_0 is the universal Kolmogoroff constant. Region of overlap II is sometimes called the inertial subrange. The functional forms given by (11) and (12) are the only ones that simultaneously satisfy the two laws applicable in each region of overlap. The boundaries of these regions of overlap are indicated in figure 2 (*a*). The constants P, N and M are universal constants and F is a large-scale characteristic constant. The relationships for these boundaries can be derived from (6), (7), (8) and (10*b*). It will be shown later that there is encouraging experimental evidence for the existence of these anticipated overlap regions. Equation (11) was deduced, using the above dimensional argument, by Perry & Abell (1977).

The analysis for the u_2 motions yields a similar set of relations with an additional set of universal constants, some of which can be related to the u_1 spectral constants in the Kolmogoroff region. For the u_3 motions, one would expect from earlier discussions that, no 'outer-flow' scaling law should result, and the various u_3 spectral regions are shown in figure 2 (*b*) with one region of overlap between an 'inner-flow' scaling law and the Kolmogoroff scaling law. Again, the u_3 spectral constants in the Kolmogoroff region can be related to the u_1 constants.

Sketches of the expected u_1 spectral distribution plotted with 'inner-flow' and 'outer-flow'-scaling coordinates are shown in figures 3 and 4 respectively. With 'inner-flow' scaling the spectra at low $k_1 z$ should peel off at $k_1 z = Fz/\Delta_E$ from an inverse-power-law region (11*a*), and, at very high $k_1 z$, peel off at $k_1 z = M\kappa^{-\frac{1}{4}}(z_+)^{\frac{3}{4}}$ from a $-\frac{5}{3}$ power law, (12*b*). Here $z_+ = zU_\tau/\nu$. With 'outer-flow' scaling the spectrum of the low-wavenumber motions, which are non-universal as regards to 'inner-flow'

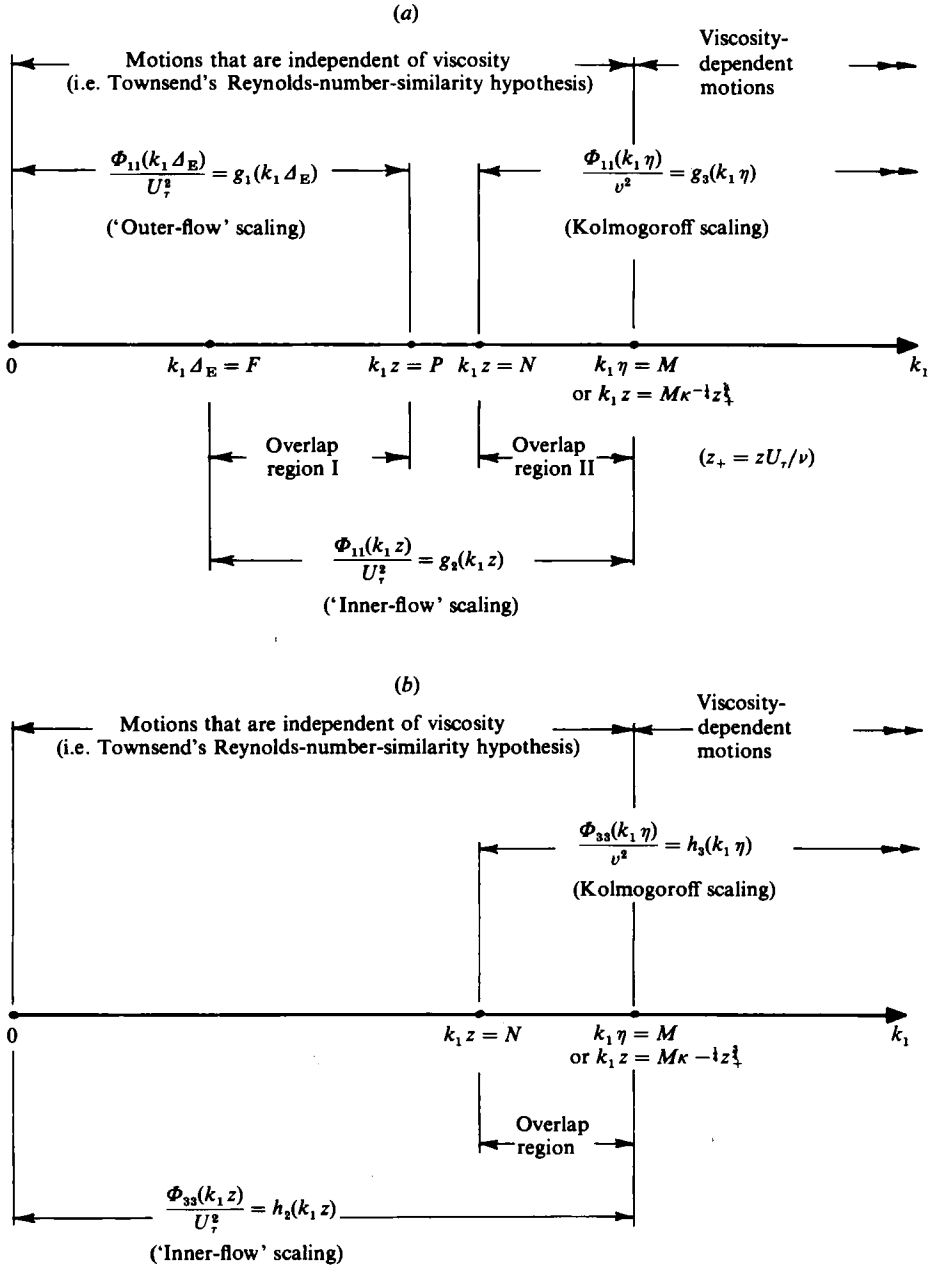

FIGURE 2. A summary of the various spectral regions for velocity fluctuations in the turbulent wall region. (*a*) u_1 spectra. (*b*) u_3 spectra.

scaling, should collapse to a universal region at low $k_1\Delta_E$. At high $k_1\Delta_E$ the spectra should peel off at $k_1\Delta_E = P\Delta_E/z$ from the inverse-power-law distribution. Figures 5 and 6 show the expected u_3 spectral distribution plotted with 'inner-flow'- and 'outer-flow'-scaling coordinates respectively. With 'inner-flow' scaling the u_3 spectra at low to high $k_1 z$ should collapse to a universal region, which at high $k_1 z$ follows a $-\frac{5}{3}$ power law from which the spectra peel off at $k_1 z = M\kappa^{-\frac{1}{4}}(z_+)^{\frac{3}{4}}$. 'Pre-multiplied'

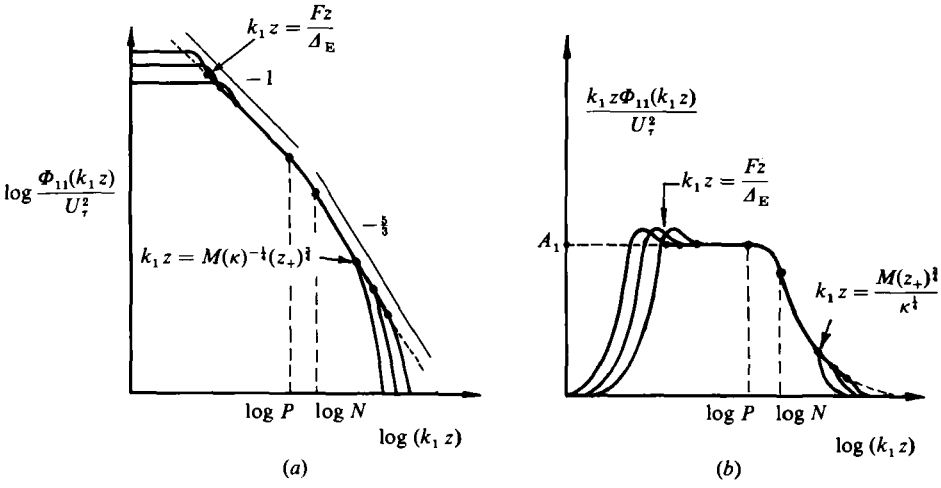

FIGURE 3. Sketches of the expected distributions of (*a*) u_1 spectra and (*b*) pre-multiplied u_1 spectra when scaled with 'inner-flow'-scaling coordinates for varying values of z/Δ_E and z_+ within the turbulent wall region.

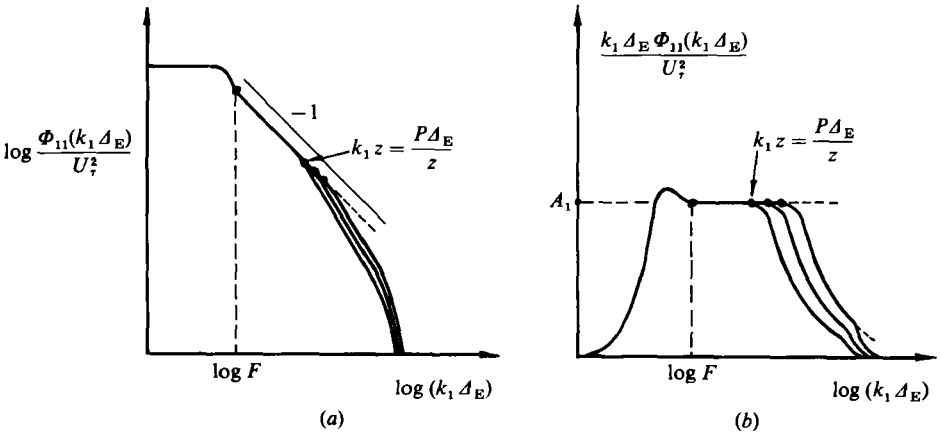

FIGURE 4. Sketches of the expected distributions of (*a*) u_1 spectra and (*b*) pre-multiplied u_1 spectra when scaled with 'outer-flow'-scaling coordinates.

spectra are also shown in the figures on semi-logarithmic plots; such plots conveniently show the non-dimensional energy contribution over any wavenumber range as an area under the curve.

Returning to the u_1 spectra, the broadband turbulence intensities can be found by integrating over the various spectral regions. With reference to figure 2(*a*) we have

$$\frac{\overline{u_1^2}}{U_\tau^2} = \int_0^F g_1(k_1 \Delta_E)\,\mathrm{d}(k_1 \Delta_E) + \int_{Fz/\Delta_E}^P g_2(k_1 z)\,\mathrm{d}(k_1 z) + \int_P^N g_2(k_1 z)\,\mathrm{d}(k_1 z) + \int_N^{M\kappa^{-\frac{1}{4}}(z_+)^{\frac{3}{4}}} g_2(k_1 z)\,\mathrm{d}(k_1 z) + \frac{\nu^2}{U_\tau^2}\int_M^\infty g_3(k_1 \eta)\,\mathrm{d}(k_1 \eta). \quad (13)$$

In (13) the first integral equals a large-scale characteristic constant; the second is evaluated using (11*a*); the third equals a universal constant; the fourth is evaluated

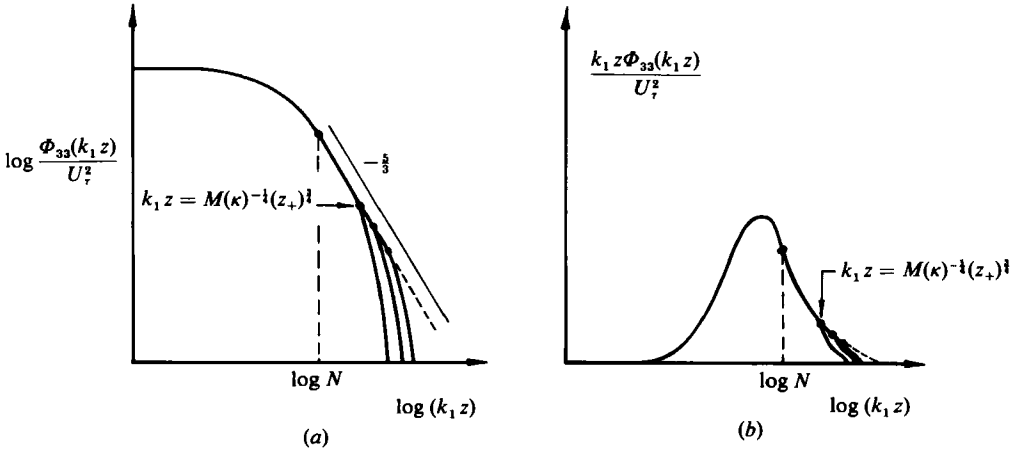

FIGURE 5. Sketches of the expected distributions of (*a*) u_3 spectra and (*b*) pre-multiplied u_3 spectra when scaled with 'inner-flow'-scaling coordinates.

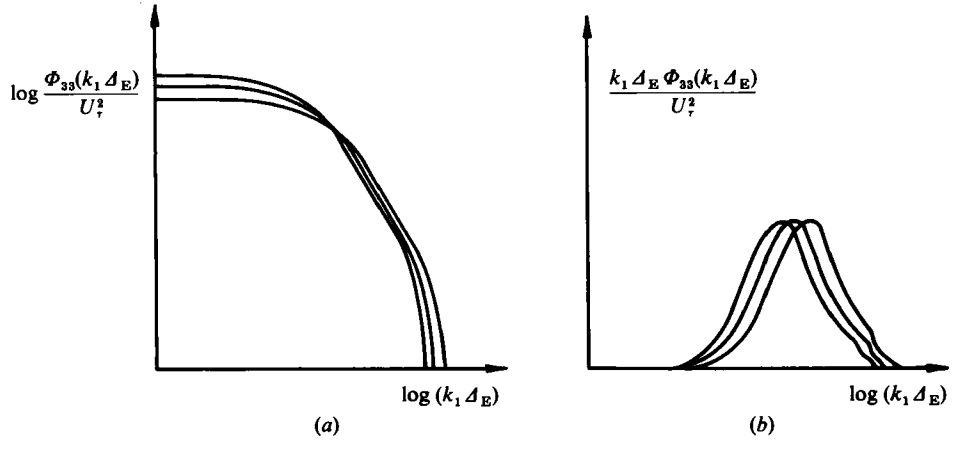

FIGURE 6. Sketches of the expected distributions of (*a*) u_3 spectra and (*b*) pre-multiplied u_3 spectra when scaled with 'outer-flow'-scaling coordinates.

using (12*b*) and the energy contribution from the last term is assumed to be negligible. This yields

$$\frac{\overline{u_1^2}}{U_\tau^2} = B_1 - A_1 \ln\left[\frac{z}{\Delta_E}\right] - C(z_+)^{-\frac{1}{2}}, \tag{14}$$

where A_1 and C are universal constants and B_1 is a large-scale characteristic constant. Similarly, for the u_2 motions,

$$\frac{\overline{u_2^2}}{U_\tau^2} = B_2 - A_2 \ln\left[\frac{z}{\Delta_E}\right] - \tfrac{4}{3}C(z_+)^{-\frac{1}{2}}, \tag{15}$$

where A_2 is a universal constant and B_2 is a large-scale characteristic constant; while for the u_3 motions

$$\frac{\overline{u_3^2}}{U_\tau^2} = A_3 - \tfrac{4}{3}C(z_+)^{-\frac{1}{2}}, \tag{16}$$

where A_3 is a universal constant. It should be noted that C occurs in all of the above equations and the factor $\frac{4}{3}$ appears from the theory of isotropic turbulence applied to the amplitudes of Φ_{11}, Φ_{22} and Φ_{33} in the inertial subrange when expressed in terms of the streamwise wavenumber k_1 (see Townsend 1976, p. 93; Batchelor 1956). Equations (14), (15) and (16) are valid provided $\nu/U_\tau \ll z \ll \Delta_E$, and in the limit as $z_+ \to \infty$ the equations reduce to those arrived at by Townsend (1976) who used broadband-turbulence-intensity arguments and neglected the fine-scale motions describable by (8).

3. A more detailed physical model for wall turbulence

3.1. *Mean-flow distribution*

Much of what follows is based on Townsend's (1976) attached eddy hypothesis and the model of PC. Consider a representative eddy of scale δ similar to those shown in figure 1 with a characteristic velocity scale U_τ. Let an array of these eddies distributed randomly in the (x, y)-plane, with average streamwise and cross-stream spacings which scale with δ, be representative of a hierarchy of scale δ, and let the contribution that this hierarchy makes to the mean cross-stream vorticity at a distance z from the wall be ξ_H. From dimensional analysis it can be shown that

$$\xi_H = \frac{U_\tau}{\delta} f\left(\frac{z}{\delta}\right). \tag{17}$$

Then the mean cross-stream vorticity at a fixed z for a range of geometrically similar hierarchies varying in scale from δ_1 to Δ_E is

$$\frac{d\overline{U_1}}{dz} = \int_{\delta_1}^{\Delta_E} \xi_H p_H(\delta)\, d\delta, \tag{18}$$

where $p_H(\delta)$ is the p.d.f. of hierarchy scales. Townsend (1976) assumed $p_H(\delta)$ to be continuous and of the form

$$p_H(\delta) = \frac{\mathcal{M}}{\delta}, \tag{19}$$

since this and the previous assumptions lead to a region of constant Reynolds shear stress for $\delta_1 \ll z \ll \Delta_E$. Here $\mathcal{M}$ is a disposable universal constant. Using (17), (18) and (19) we obtain

$$\frac{dU_D^*}{d\lambda_E} = \int_{\lambda_1}^{\lambda_E} \mathcal{M} h(\lambda) e^{-\lambda}\, d\lambda, \tag{20}$$

where $U_D^* = (\overline{U_{1E}} - \overline{U_1})/U_\tau$, the non-dimensional mean-velocity defect. Also,

$$\lambda = \ln(\delta/z); \quad \lambda_1 = \ln(\delta_1/z); \quad \lambda_E = \ln(\Delta_E/z) \quad \text{and} \quad h(\lambda) = f(z/\delta).$$

It can be shown that

$$U_D^* = \int_0^{\lambda_E} \int_{\lambda_1}^{\lambda_E} \mathcal{M} h(\lambda) e^{-\lambda}\, d\lambda\, d\lambda_E. \tag{21}$$

By assuming that all the vorticity is confined to the vortex loop and that the surrounding fluid is irrotational, PC were able to relate various forms of $h(\lambda)$ or $f(z/\delta)$ to the representative eddy geometry. We shall now examine various forms of $h(\lambda)$ and compare the resulting U_D^* distributions with the Hama (1956) velocity-defect-law

distribution in a zero-pressure-gradient turbulent boundary layer on a flat plate. This empirical law in terms of our logarithmic variables is

$$\left.\begin{aligned} U_{\mathrm{D}}^{*} &= K(1-\mathrm{e}^{-\lambda_{\mathrm{E}}})^{2} \quad \left(0 \leqslant \lambda_{\mathrm{E}} \leqslant \ln\left(\frac{1}{0.15}\right)\right), \\ &= \frac{1}{\kappa}\lambda_{\mathrm{E}} + D \qquad \left(\lambda_{\mathrm{E}} \geqslant \ln\left(\frac{1}{0.15}\right)\right), \end{aligned}\right\} \tag{22}$$

where the constants K and D are 9.6 and 2.309 respectively. Alternatively, we could have used the Coles (1956) 'law-of-the-wall' and 'law-of-the-wake' formulation to generate the velocity-defect law. Equation (22) is shown as one of the curves plotted in figure 8.

Figure 7 shows 'representative eddies' of various geometries and their $f(z/\delta)$ and $h(\lambda)\,\mathrm{e}^{-\lambda}$ distributions, and their resulting U_{D}^{*} distributions are shown in figure 8. All cases shown lead to the expected logarithmic distribution in U_{D}^{*} for λ_{E} sufficiently large. The constant $\mathscr{M}$ in (19), (20) and (21) is evaluated using the condition $(\mathrm{d}U_{\mathrm{D}}^{*}/d\lambda_{\mathrm{E}}) \to 1/\kappa$ for $\lambda_{\mathrm{E}} \gg 0$ and $\lambda_{1} \leqslant 0$. Case (*a*), a Λ-shaped vortex, where all the cross-stream vorticity is confined to the top of the vortex loop, gives a logarithmic distribution through the layer and its intercept is zero at $\lambda_{\mathrm{E}} = 0$. Case (*b*), a Λ-shaped vortex, where the cross-stream vorticity is distributed uniformly over the height of the eddy, gives a negative intercept for the logarithmic distribution at $\lambda_{\mathrm{E}} = 0$.

If we equate $\mathrm{d}^{2}U_{\mathrm{D}}^{*}/\mathrm{d}\lambda_{\mathrm{E}}^{2}$ determined from (20) and (22), it is possible to find the appropriate $h(\lambda)$ or $f(z/\delta)$ which yields the Hama distribution in the region $0 \leqslant \lambda_{\mathrm{E}} \leqslant -\ln(0.15)$. This gives the 'bow-legged' parabolic eddy shown in figure 7(*c*). This eddy geometry seems unlikely.

To consider that a hierarchy can be represented by a single realizable eddy is a simplification. Rather, in accordance with PC, it would be more realistic to regard a hierarchy as consisting of an assemblage of eddies at different stages of stretching as shown in figure 7(*d*, *e*). Case (*d*) shows a Λ-vortex undergoing a plane-strain-like motion, as was indicated by the Biot–Savart-law calculations of PC. The eddy starts at a height $b\delta$ and is stretched to a height δ, where it either pairs with another similar eddy to form the shortest eddy of the next hierarchy or viscous diffusion and vorticity cancellation causes eddy 'death'. Case (*e*) shows an assemblage of Π-shaped vortices at different stages of stretching. The U_{D}^{*} distributions for these two cases for $b = 0.5$ are also shown in figure 8. For each case we obtain the correct logarithmic distribution for λ_{E} large, but the extrapolated intercept is still negative. From a study of experimental spectra (presented in §4.2.1) the authors propose that, instead of varying the eddy geometry, the inverse-power-law p.d.f. should be modified by increasing the weighting for the large-scale eddies, as shown in figure 9(*a*). The large-scale eddies need not be geometrically similar to the smaller-scale attached eddies, which are responsible for the logarithmic mean-velocity distribution in the turbulent wall region. However, as a first approximation, it will be assumed here that the large-scale eddies with this additional weighting are geometrically similar to the smaller-scale ones. The type of modification shown in figure 9(*a*) will give the correct type of behaviour for the Hama velocity-defect-law formulation (i.e. a positive extrapolated intercept). A simplified modification is shown in figure 9(*b*) and this is equivalent to multiplying the inverse-power-law p.d.f. with a weighting function $W(\delta/\Delta_{\mathrm{E}})$, shown in figure 9(*c*), such that

$$p_{\mathrm{H}}(\delta) = \frac{\mathscr{M}}{\delta} W\left[\frac{\delta}{\Delta_{\mathrm{E}}}\right]. \tag{23}$$

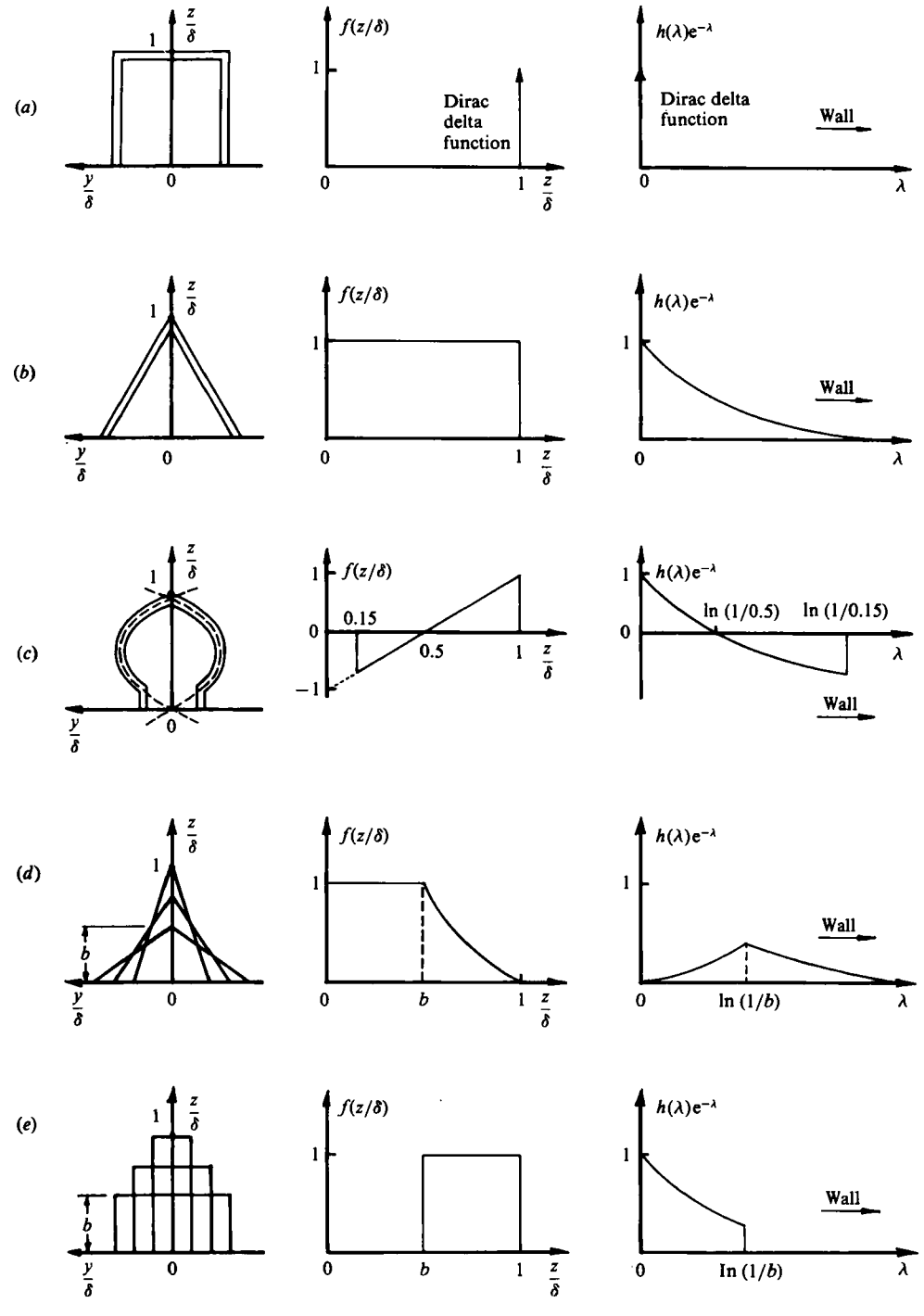

FIGURE 7. Projections in the (y, z)-plane of various representative eddy geometries together with their $f(z/\delta)$ and $h(\lambda)e^{-\lambda}$ distributions. (*a*) $\sqcap$-eddy; (*b*) $\wedge$-eddy; (*c*) bow-legged, parabolic eddy; (*d*) stretched $\wedge$-eddy; (*e*) stretched $\sqcap$-eddy.

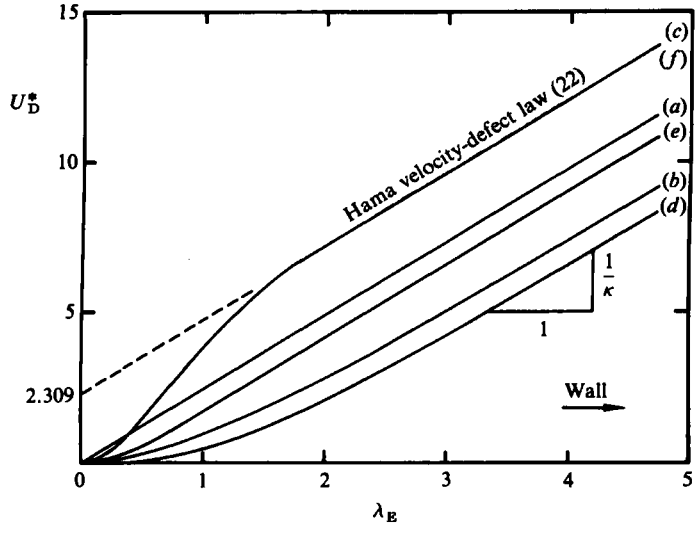

FIGURE 8. The resulting U_D^* distributions for each of the representative eddy geometries shown in figure 7 compared with the Hama (1954) velocity-defect-law formulation. Case (*f*) is for a stretched $\sqcap$-eddy with a weighting function ($a = 4.586$, $d = 0.588$ and $b = 0.263$).

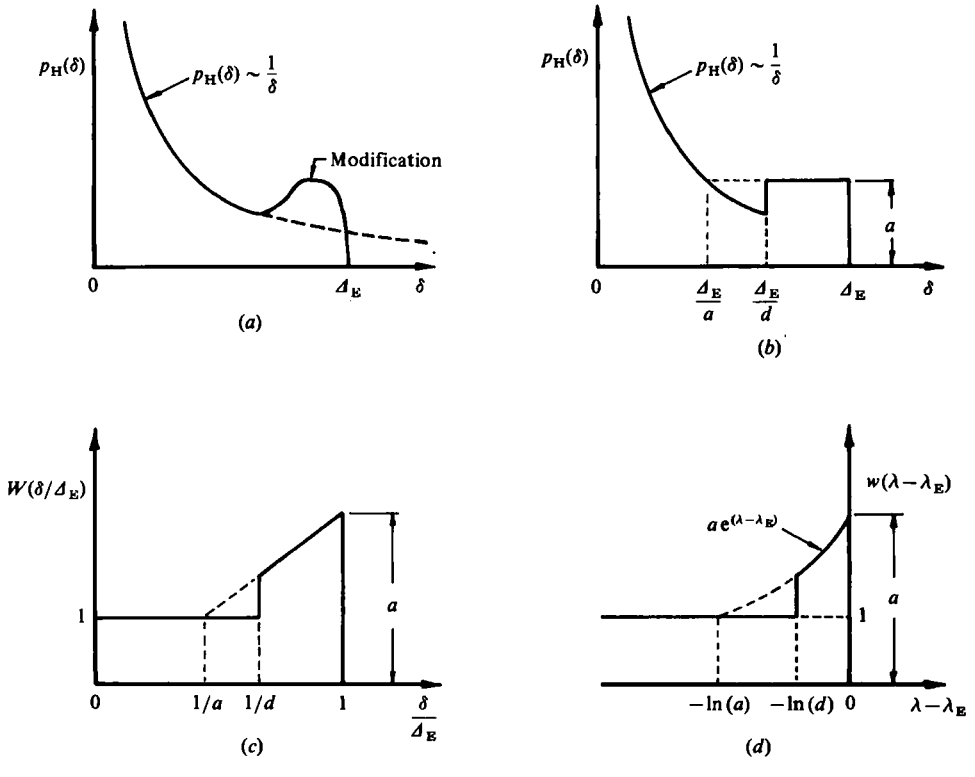

FIGURE 9. (*a*) The type of modification to $p_H(\delta)$ needed to obtain the Hama (1954) velocity-defect law. (*b*) A simplified modification. (*c*) The corresponding weighting function, $W(\delta/\Delta_E)$. (*d*) $w(\lambda-\lambda_E) = W(\delta/\Delta_E)$.

Figure 9(*d*) shows this function with logarithmic variables, where

$$w(\lambda-\lambda_{\mathrm{E}}) = W(\delta/\Delta_{\mathrm{E}}).$$

With this modification (20) becomes

$$\frac{\mathrm{d}U_{\mathrm{D}}^*}{\mathrm{d}\lambda_{\mathrm{E}}} = \int_{\lambda_1}^{\lambda_{\mathrm{E}}} \mathscr{M} h(\lambda)\,\mathrm{e}^{-\lambda}\, w(\lambda-\lambda_{\mathrm{E}})\,\mathrm{d}\lambda. \tag{24}$$

This is an integral equation similar to those used for solving inverse-scattering problems. Given $\mathrm{d}U_{\mathrm{D}}^*/\mathrm{d}\lambda_{\mathrm{E}}$ and $w(\lambda-\lambda_{\mathrm{E}})$, the problem is to determine $h(\lambda)$. However, since the precise form of $w(\lambda-\lambda_{\mathrm{E}})$ is unknown, we must resort to trial and error. Figure 10 shows how the integral in (24) is carried out for trial distributions of $h(\lambda)\,\mathrm{e}^{-\lambda}$ and $w(\lambda-\lambda_{\mathrm{E}})$. The shaded area equals $\mathrm{d}U_{\mathrm{D}}^*/\mathrm{d}\lambda_{\mathrm{E}}$ and the width of the integration window, $\lambda_{\mathrm{E}}-\lambda_1$, is fixed for a given Reynolds number since $\lambda_{\mathrm{E}}-\lambda_1 = \ln(\Delta_{\mathrm{E}}\,U_\tau/\nu)+Q$, where Q is a universal constant. In (24) we must ensure that $\lambda_1 \leqslant 0$, since, as PC indicated, a special formulation is needed for the smallest hierarchy to include the additional non-geometrically-similar eddies forming from the roll-up of viscous sublayer material. For simplicity consider the case of an assemblage of stretched Π-eddies as shown in figure 7(*e*). Values of $a = 4.568$ and $d = 0.588$ (defined in figure 9) and $b = 0.263$ give a U_{D}^* distribution which fits the Hama formulation reasonably well as seen in figure 8. This modification of the p.d.f. by a weighting function has important implications in spectra and broadband turbulence intensities as outlined in the following sections.

3.2. *Turbulence spectra*

Let the power-spectral density of u_i velocity fluctuations, area-averaged in a plane at a distance z from the wall, for a hierarchy of scale δ be $\phi_{ii}(k_1 z, z/\delta)$. This will be called the hierarchy spectral function. Then, the summed power-spectral density at a fixed z for a range of hierarchy scales varying from δ_1 to Δ_{E} is given by

$$\frac{\Phi_{ii}(k_1 z, z/\Delta_{\mathrm{E}}, z/\delta_1)}{U_\tau^2} = \int_{\delta_1}^{\Delta_{\mathrm{E}}} \frac{\phi_{ii}(k_1 z, z/\delta)}{U_\tau^2}\, p_{\mathrm{H}}(\delta)\,\mathrm{d}\delta. \tag{25}$$

To be consistent with the mean-flow work in §3.1, we shall assume that $p_{\mathrm{H}}(\delta)$ is given by (23). Then pre-multiplying (25) by $k_1 z$ enables this equation to be written in terms of our logarithmic arguments, thus

$$F_{ii}(\alpha_z, \lambda_{\mathrm{E}}, \lambda_1) = \int_{\lambda_1}^{\lambda_{\mathrm{E}}} \mathscr{M}\, \frac{\psi_{ii}(\alpha,\lambda)}{U_\tau^2}\, w(\lambda-\lambda_{\mathrm{E}})\Big|_{k_1 z=\text{const.}} \mathrm{d}\lambda, \tag{26}$$

where $\alpha = \ln(k_1\delta)$, $\alpha_z = \ln(k_1 z)$, $F_{ii} = k_1 z \Phi_{ii}/U_\tau^2$ and $\psi_{ii} = k_1 z \phi_{ii}$. We shall call ψ_{ii} the pre-multiplied hierarchy spectral function. In (26) we are integrating with respect to δ with all other parameters fixed, in particular $k_1 z$.

The functions ψ_{ii} have been calculated for a hierarchy consisting of a random array (in the (x,y)-plane) of Λ-shaped vortices of the same scale. For simplicity the effect of stretching, as illustrated in figure 7(*d*, *e*), has not been included. Figure 11 shows the proportions of the Λ-vortex used together with the image vortex. The vorticity distribution in the vortex rods is assumed to be Gaussian (see PC, §2) with a characteristic lengthscale $r_0 = 0.10\delta$. The function ψ_{ii} was computed by taking fast Fourier transforms of u_i velocity distributions, induced by one isolated Λ-vortex and its image, along lines of constant y/δ in a plane of constant z/δ. The velocity distributions were calculated using the Biot–Savart law. The power-spectral density

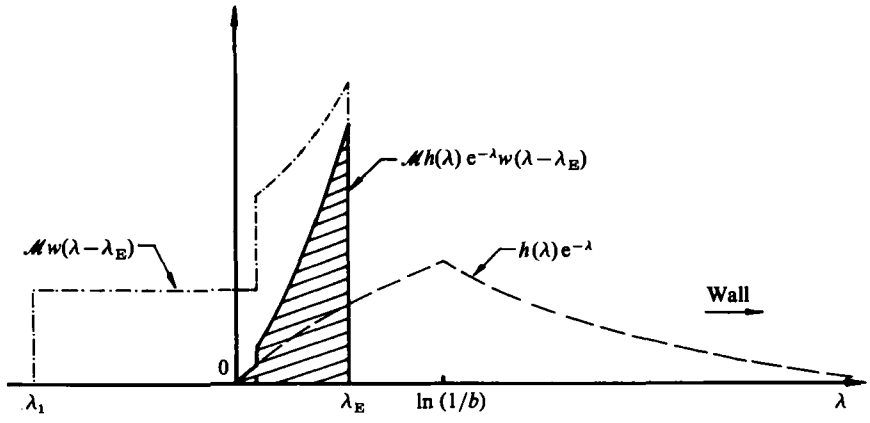

FIGURE 10. The evaluation of equation (24).

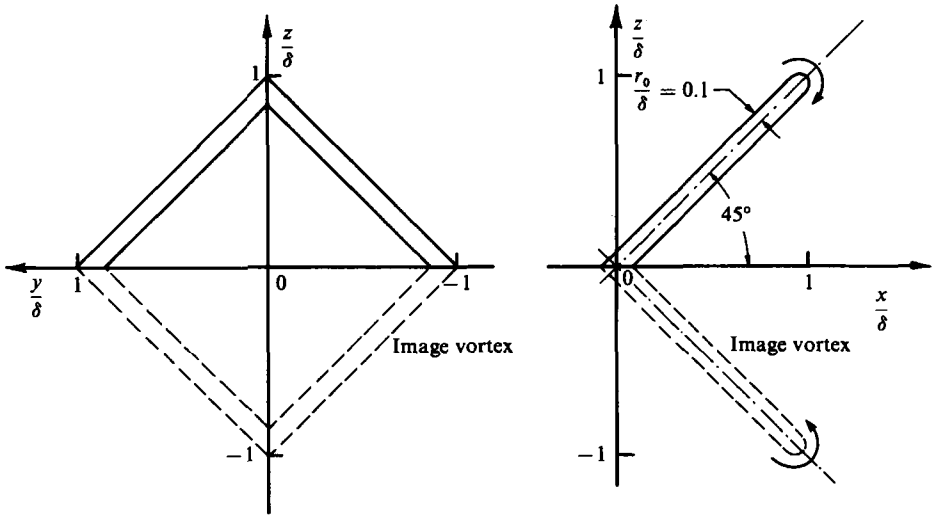

FIGURE 11. -vortex geometry used to calculate ψ_{ii}/U_τ^2.

for a random array of such vortices was formed by ensemble averaging the square of the moduli of the fast Fourier transform of the velocity signatures in the plane z/δ = constant for various y/δ, assuming that the mean streamwise and cross-stream densities of these vortices scale with δ. This result was pre-multiplied by $k_1 z$ to give ψ_{ii}. Sketches of the distributions of ψ_{11}/U_τ^2, ψ_{22}/U_τ^2 and ψ_{33}/U_τ^2 are presented in the form of 'contour maps' in figure 12 (*a–c*), respectively. It can be seen that the contours of ψ_{11} and ψ_{22} are similar and considerably different from the ψ_{33} contours. For λ sufficiently large (i.e. $z/\delta \to 0$), the ψ_{11} and ψ_{22} contours run parallel to the λ-axis and are thus invariant with λ in this region, while the ψ_{33} contours asymptote to zero; as long as the Townsend boundary condition (that at $z = 0$, $u_3 = 0$ while u_1 and u_2 remain finite) is upheld, the contours will behave in the manner described for λ large, no matter what shape of eddy or assemblage of eddies is used to represent a hierarchy. For λ sufficiently negative, all contours asymptote to zero, since the far-field effect of the vortices in the hierarchy vanishes for $z \gg \delta$.

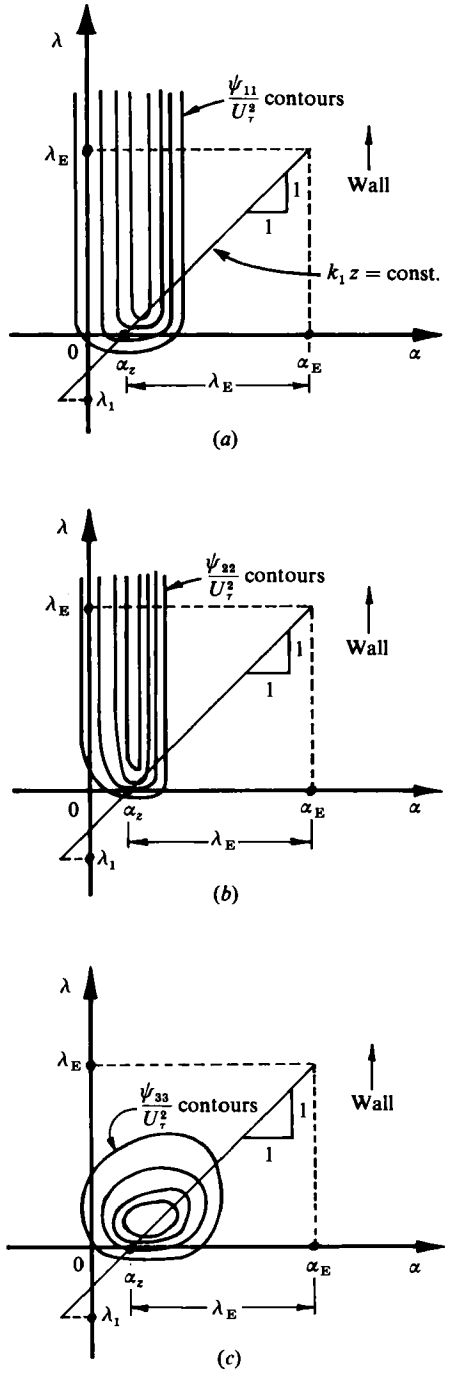

FIGURE 12. Sketches of the contours of $\psi_{ii}(\alpha, \lambda)/U_\tau^2$. (*a*) ψ_{11}/U_τ^2; (*b*) ψ_{22}/U_τ^2; (*c*) ψ_{33}/U_τ^2.

In these figures, lines of constant $k_1 z$ are given by

$$\lambda = \alpha - \alpha_z,$$

i.e. lines of slope $+1$ with an intercept of α_z on the α-axis. Imagine a plane perpendicular to the (λ, α)-plane and aligned along the line of constant $k_1 z$. This will cut through the spectral 'hill' $\psi_{ii}(\alpha, \lambda)/U_\tau^2$ and a projection of this cut is made onto the $(\psi_{ii}/U_\tau^2, \lambda)$ plane. Then weighting this projection with $\mathscr{M}w(\lambda - \lambda_E)$ and integrating between λ_1 and λ_E gives the summed non-dimensional energy-density contribution to F_{ii} at a fixed $k_1 z$ (i.e. fixed α_z) for a fixed value of λ_E (i.e. fixed z/Δ_E). This is shown clearly in figure 13(*a*). In what follows, λ_1 will be taken to be sufficiently negative and hence (26) becomes independent of λ_1. Let α_z vary from $-\infty$ to $+\infty$ with λ_E fixed. Thus $F_{ii}(\alpha_z, \lambda_E)$ can be mapped out for various values of λ_E. Such a plot would correspond to 'inner-flow' scaling of the pre-multiplied spectrum of u_i velocity fluctuations. The resulting distributions of F_{11} and F_{22} are similar to the distribution of $k_1 z \Phi_{11}(k_1 z)/U_\tau^2$ shown in figure 3(*b*) and the distribution of F_{33} is similar to the distribution of $k_1 z \Phi_{33}(k_1 z)/U_\tau^2$ shown in figure 5(*b*); however, no Kolmogoroff region exists nor does a viscous cutoff occur. Instead, at high $k_1 z$, F_{11}, F_{22} and F_{33} each collapse to their universal curve which extends to infinite $k_1 z$.

In figure 12, lines of constant $k_1 z$ also correspond to lines of constant $k_1 \Delta_E$. If we let $\alpha_E = \ln(k_1 \Delta_E)$, then the 'outer-flow'-scaling plots of the pre-multiplied spectra, $H_{ii}(\alpha_E, \lambda_E) = k_1 \Delta_E \Phi_{ii}(k_1 \Delta_E)/U_\tau^2$, can be obtained. The distributions of H_{11} and H_{22} are similar to the distribution of $k_1 \Delta_E \Phi_{ii}(k_1/\Delta_E)/U_\tau^2$ shown in figure 4(*b*) and the distribution of H_{33} is similar to the distribution of $k_1 \Delta_E \Phi_{33}(k_1 \Delta_E)/U_\tau^2$ shown in figure 6(*b*).

Figures 13(*a*), (*b*) respectively show a comparison between ψ_{11}/U_τ^2 for the present example of a Λ-vortex with its image and for the example used by PC. PC were interested only in the u_1 spectra and used an infinite straight-line vortex of some fixed orientation to generate the velocity signatures via the Biot–Savart law. Such a model does not have the correct boundary conditions for the u_3 velocity fluctuations, whereas the Λ-vortex with its image does. PC also assumed that ψ_{11}/U_τ^2 dropped suddenly to zero, for z exceeding δ, as shown in figure 13(*b*). The problem of an isolated vortex having infinite kinetic energy spread over the entire flow field at a fixed value of z was overcome by the use of an artificial outer limit on the integral used for obtaining the ensemble-averaged power-spectral density. In the case of the Λ-vortex model, this problem does not arise since it has finite energy. Also, instead of using a continuous inverse-power-law p.d.f., PC used a discrete p.d.f. where the hierarchy scales went in a geometric progression with a factor of 2. This was thought to be consistent with vortex pairing, where the lengthscales and the circulation doubled from one hierarchy to the next. It will be seen later that the use of a continuous inverse-law p.d.f. gives much the same answer. Hence we could equally well use a geometric progression with a factor of $2^{1/r}$, where r is a resolution factor. The above approach is equivalent to multiplying the integrand in (26) by a series of uniformly spaced unit Dirac delta functions, which changes the integral into a summation. This is equivalent to using a trapezoidal rule. In spite of the crudity of the PC analysis, the results produced are remarkably similar to those of the more-refined analysis presented here and are found to be insensitive to r provided $r \geqslant 1$. The PC analysis for u_1 spectra with a discrete p.d.f. with a resolution factor r will be used in the analysis given in later sections because of its analytical simplicity.

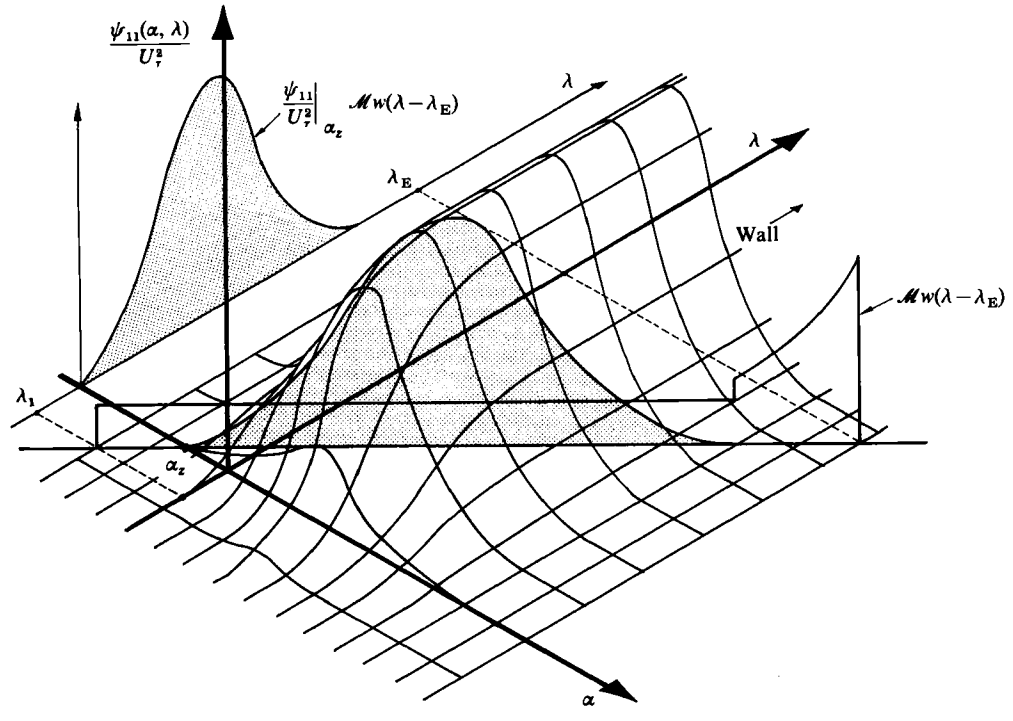

(*a*)

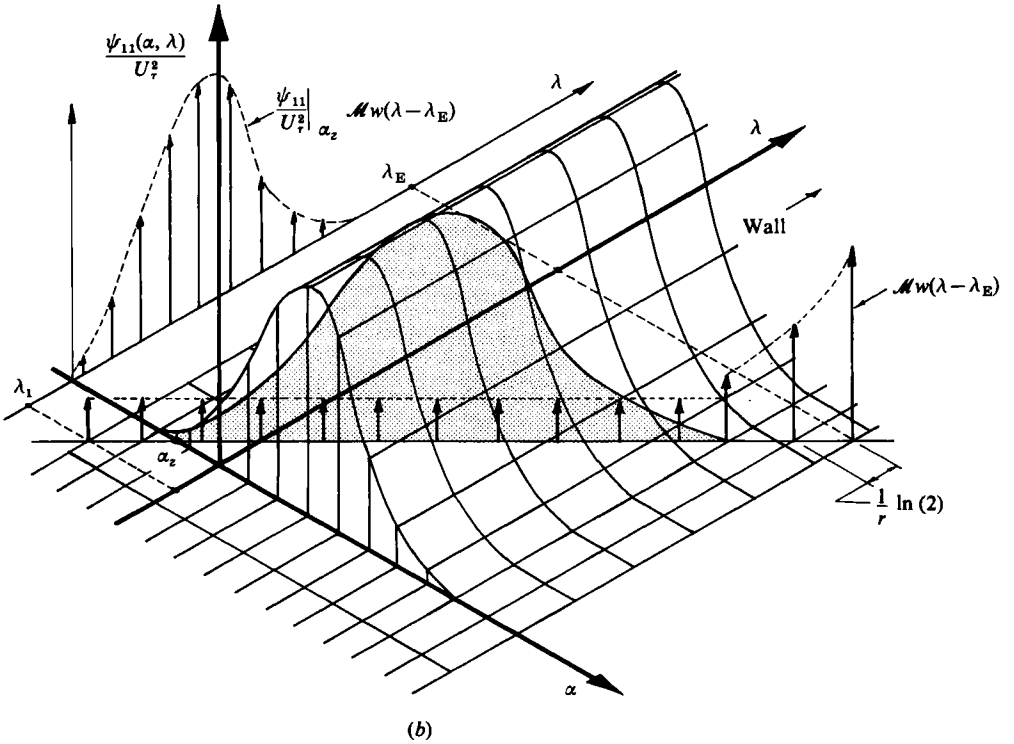

(*b*)

FIGURE 13. (*a*) The distribution of $\psi_{11}(\alpha,\lambda)/U_\tau^2$ computed for the Λ-vortex case shown in figure 11. (*b*) The distribution of $\psi_{11}(\alpha,\lambda)/U_\tau^2$ for the model of Perry & Chong (1982).

3.3. *Turbulence intensities*

Following Townsend (1976) and PC, the broadband turbulence-intensity distribution for a range of scales of geometrically similar hierarchies is given by

$$\frac{\overline{u_i u_j}}{U_\tau^2} = \int_{\delta_1}^{\Delta_E} I_{ij}\left(\frac{z}{\delta}\right) p_H(\delta)\,\mathrm{d}\delta, \tag{27}$$

where $I_{ij}(z/\delta)$ is the Townsend eddy-intensity function for a hierarchy of scale δ. The boundary conditions mentioned earlier given I_{11} and I_{22} constant and finite for $z/\delta \to 0$, $I_{13} \sim (z/\delta)$ and $I_{33} \sim (z/\delta)^2$. Townsend also assumed that, for $z \gg \delta$, $I_{ij}(z/\delta)$ asymptotes to zero. Typical distributions of $I_{ij}(z/\delta)$ shown in figure 14 highlight these functional properties.

Following the previous mean-flow and spectral analyses (§§3.1 and 3.2), it will be assumed that $p_H(\delta)$ is given by (23). Then (27) can be rewritten in the form

$$\frac{\overline{u_i u_j}}{U_\tau^2} = \int_{\lambda_1}^{\lambda_E} \mathscr{M} I_{ij}(\lambda)\, w(\lambda - \lambda_E)\,\mathrm{d}\lambda, \tag{28}$$

where the argument of the eddy-intensity function has been changed to λ. $I_{ij}(\lambda)$ can be calculated from the pre-multiplied spectral hierarchy function ψ_{ij}/U_τ^2 using

$$I_{ij}(\lambda) = \int_{-\infty}^{\infty} \frac{\psi_{ij}(\alpha, \lambda)}{U_\tau^2}\,\mathrm{d}\alpha.$$

Figure 15(*a*, *b*) shows $I_{11}(\lambda)$ and $I_{33}(\lambda)$ calculated from ψ_{ij}/U_τ^2 obtained for the Λ-vortex model used in §3.2. The distribution of $I_{22}(\lambda)$ will be similar to that for $I_{11}(\lambda)$, in that they are both finite and constant for $\lambda \gg 0$, and the distribution of $I_{13}(\lambda)$ will be similar to $I_{33}(\lambda)$, in that they both have finite area. Also shown in the figure is a weighting function $w(\lambda - \lambda_E)$. It can be seen from figure 15(*a*, *b*) and the above comments that, for λ_E sufficiently large and λ_1 sufficiently less that zero, (28) must lead to

$$\frac{\overline{u_1^2}}{U_\tau^2} = A_1 \lambda_E + B_1, \tag{29a}$$

$$\frac{\overline{u_2^2}}{U_\tau^2} = A_2 \lambda_E + B_2, \tag{29b}$$

$$\frac{\overline{u_3^2}}{U_\tau^2} = A_3, \tag{29c}$$

$$\frac{\overline{u_1 u_3}}{U_\tau^2} = K_{13}. \tag{29d}$$

A_1, A_2, A_3 and K_{13} are universal constants. In fact, it can be shown that

$$\left.\begin{aligned} A_1 &= \mathscr{M} I_{11} \quad (z/\delta = 0), \\ A_2 &= \mathscr{M} I_{22} \quad (z/\delta = 0), \\ A_3 &= \int_0^\infty \mathscr{M} I_{33}(\lambda)\,\mathrm{d}\lambda, \\ K_{13} &= \int_0^\infty \mathscr{M} I_{13}(\lambda)\,\mathrm{d}\lambda = -1, \end{aligned}\right\} \tag{30}$$

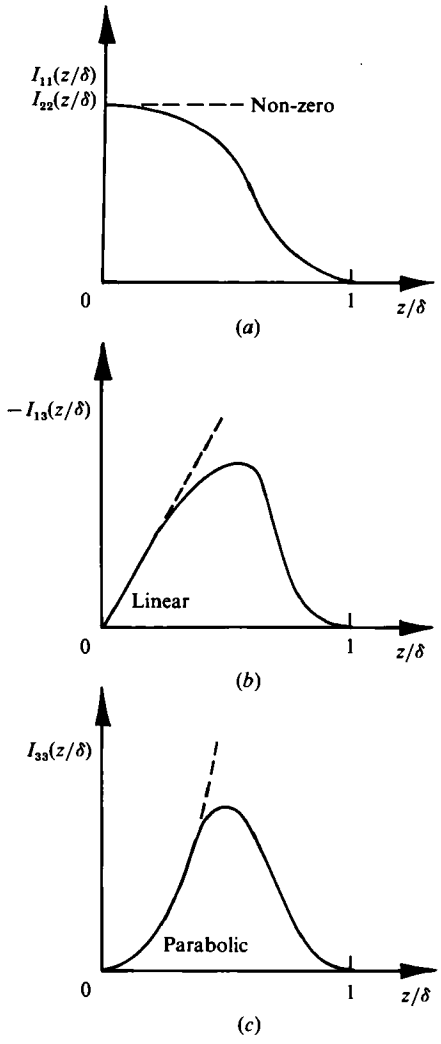

FIGURE 14. Typical eddy-intensity functions. (a) $I_{11}(z/\delta)$; (b) $I_{13}(z/\delta)$; (c) $I_{33}(z/\delta)$.

In (29), B_1 and B_2 are large-scale characteristic constants which depend on the form of $w(\lambda-\lambda_E)$. The equations listed in (29) are the result obtained by Townsend (1976) and by PC, and are the same as (14), (15) and (16) using the dimensional-analysis arguments given in §2 if the fine-scale motions are neglected or if $z_+ \to \infty$.

The analysis presented in this detailed physical model of wall turbulence is applicable only to flat-plate flow with a zero streamwise pressure gradient. Fully developed flow in ducts and pipes would have the complicating feature of eddies intruding from the opposite boundary, and in a pipe curvature effects would also influence the large-scale motions. However, as indicated in the dimensional-analysis arguments given earlier, the preceding analysis should be applicable in the turbulent wall region in pipes and ducts. This is substantiated experimentally for pipes in the next section. Much of the difference between the various flow geometries can be accounted for by an appropriate modification to the weighting function $w(\lambda-\lambda_E)$. This in turn will control the values of the large-scale characteristic constants given

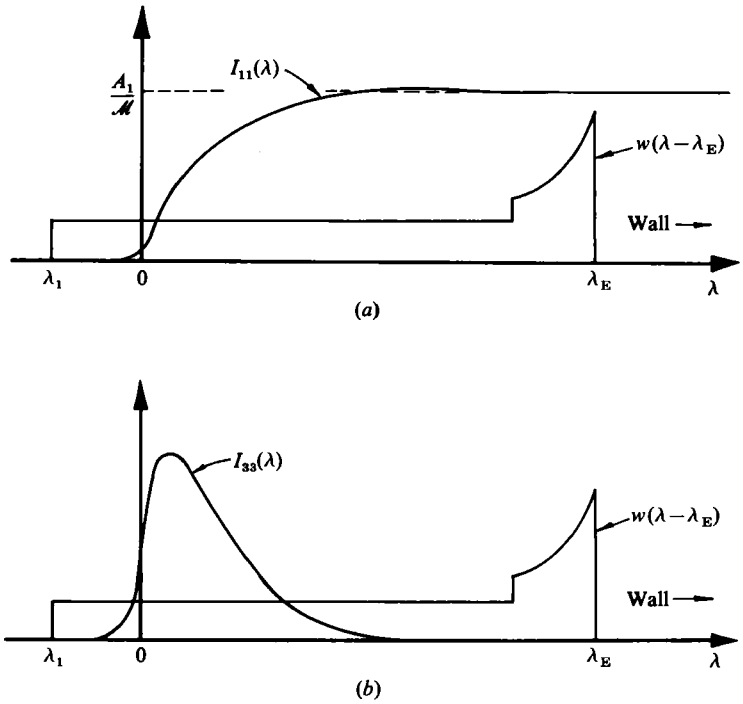

FIGURE 15. Distributions of (*a*) $I_{11}(\lambda)$ and (*b*) $I_{33}(\lambda)$ calculated from the computed distributions of ψ_{11}/U_τ^2 and ψ_{33}/U_τ^2 for the Λ-vortex shown in figure 11.

in §2 and the distribution of low-wavenumber energy of the u_1 and u_2 spectra. Furthermore, it is argued that, although there will be detailed differences between the geometries for flow beyond the turbulent wall region, the general form of the scaling laws will still be applicable to all flow geometries.

4. Experimental results

4.1. *Apparatus and method*

The results presented here were obtained in fully developed, turbulent flow in a smooth-walled circular pipe. The pipe consisted of seven 6 m lengths of precision-drawn brass tubing of 0.099 m internal diameter. Adjacent lengths were joined using specially machined collars which ensured that the surface discontinuities at the joints were minimal. The contraction used is described in Perry & Abell (1975) and a sandpaper trip was used after the contraction to stabilize the transition of the flow to turbulence.

All measurements were taken 398.5 diameters downstream from the pipe entrance and hopefully this ensured that the flow was fully developed. The flow was examined over the range of Reynolds numbers ($Re = 2\Delta_E \overline{U_{1E}}/\nu$) of 75000 to 200000, which corresponded to a Kármán-number ($\Delta_E U_\tau/\nu$) range of 1610 to 3900. The wall-shear velocity U_τ was determined from the static-pressure drop per unit length along the pipe. All measurements, including the hot-wire results, were corrected for the effect of the density variation of the air along the length of the pipe. Temperature corrections were not necessary.

Turbulence measurements were obtained using constant-temperature hot-wire

anemometers similar to those used by Perry & Morrison (1971). The hot-wire filaments were made from 5 μm Wollaston wire and had nominal etched lengths of 0.90 mm. The wires were calibrated dynamically by following the method outlined in §8.6 of Perry (1982). The dynamic calibration facility used enabled the wires to be calibrated inside the pipe at the test section. During calibration the wires were exposed to a turbulent free uniform stream by removing the length of the pipe upstream from the test section and replacing it with a contraction with screens. The dynamic calibration facility contained the traversing mechanism and this ensured that the orientation of the wires during calibration was the same as that during measurement.

The u_1 spectra were measured using uncalibrated normal wires and u_3 spectra using dynamically matched, uncalibrated X-wires. The power-spectral density of the pertinent anemometer signal was calculated digitally using a FFT algorithm. The signal was low-pass filtered at half the digital sampling rate (using Krohn–Hite analog filters model number 3323) to ensure that no aliasing of the measured spectrum occurred. The ensemble average of ten such power-spectral densities gave sufficient convergence of the spectrum after a 'smoothing window' had been applied. The final spectrum covered a frequency range from 2 to 10 kHz. The argument of the spectrum was transformed from circular frequency to streamwise wavenumber by applying Taylor's (1938) hypothesis of frozen turbulence and assuming that all eddies moved at a convection velocity equal to the local mean velocity $\overline{U_1}$ at the measuring point. Zaman & Hussain (1981) from their investigation of the applicability of the Taylor hypothesis were led to state that 'the use of the local time-average velocity in shear flows especially in the computation of wavenumber spectra and the eduction of large scale structures is not acceptable'. The applicability of this hypothesis is investigated further in §4.2.1. All spectra were normalized using (5) and it was assumed for the purposes of normalization that at low wavenumbers the measured spectrum could be extrapolated with $\Phi_{ii}(k_1)$ constant and at high wavenumbers with $\Phi_{ii}(k_1) \propto k_1^{-4}$.

In the turbulent wall region, the turbulent energy dissipation ϵ was calculated using (3), (9) and that for a pipe

$$-\frac{\overline{u_1 u_3}}{U_\tau^2} = 1 - \frac{z}{\Delta_E}. \tag{31}$$

In the wake region, the assumption that production is in balance with dissipation is no longer valid, so it was necessary to resort to

$$\epsilon = 15\nu \int_0^\infty k_1^2 \Phi_{11}(k_1)\, \mathrm{d}k_1, \tag{32}$$

which assumes isotropy of the dissipating motions. It can be shown that (32) leads to large errors in the value of ϵ if $\eta < \ell$, where ℓ is the smallest-scale motion that the hot-wire(s) can resolve.

4.2. *Experimental turbulence spectra*

4.2.1. *The turbulent wall region*†

(i) u_1 spectra. Spectra of u_1 velocity fluctuations measured in the turbulent wall region are shown in figure 16(*a*) with 'inner-flow'-scaling coordinates for various values of z/Δ_E for normal wires of lengths $l = 0.39$ and 1.26 mm. The data appear

† For a pipe the turbulent wall region is tentatively defined here as $140\nu/U_\tau \leqslant z \leqslant 0.14\Delta_E$.

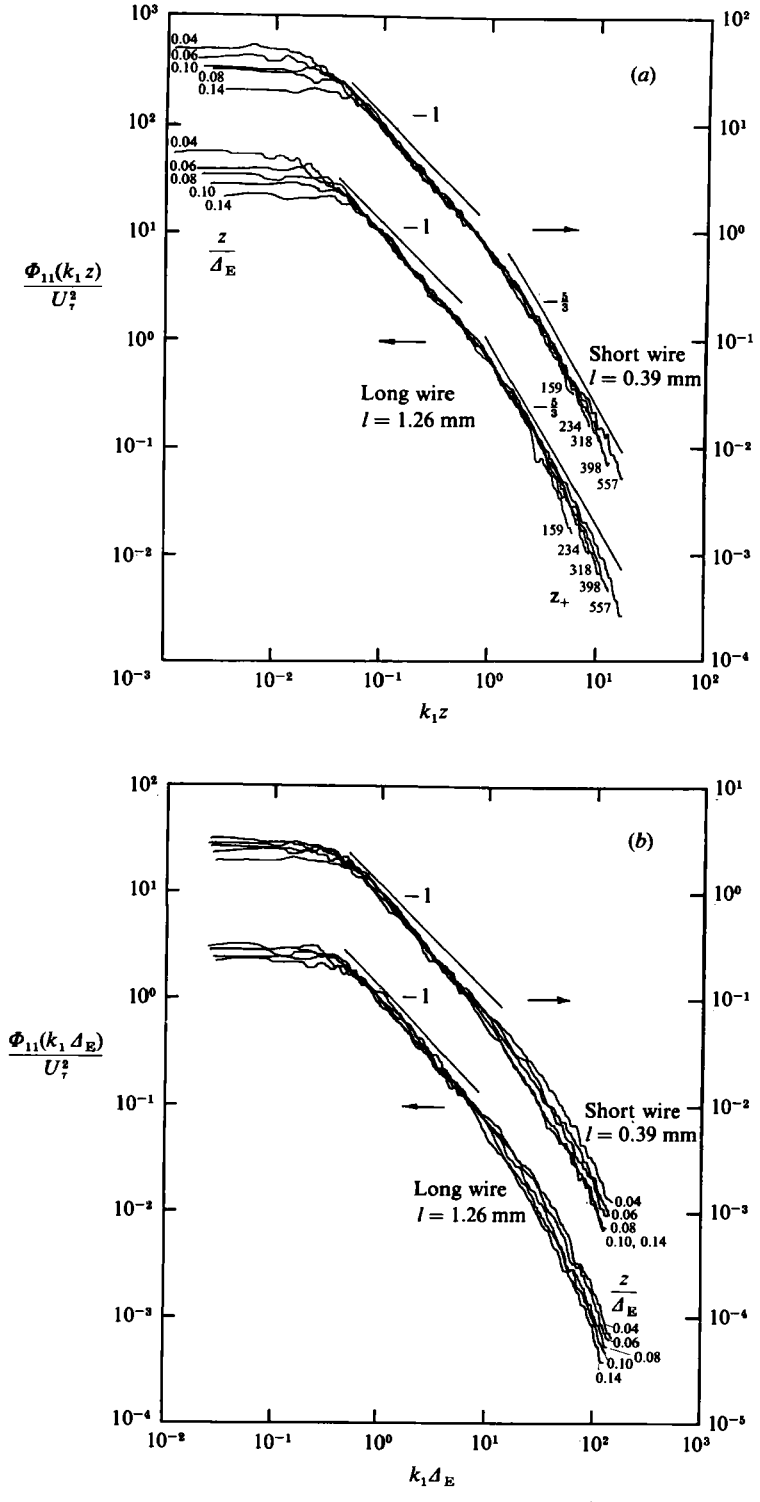

FIGURE 16. (*a*) u_1 spectra scaled with 'inner-flow'-scaling coordinates for varying values of z/Δ_E within the turbulent wall region. $Re = 200000$. (*b*) The same scaled with 'outer-flow'-scaling coordinates.

to be consistent with the expected distributions shown in figure 3(*a*). The data are shown scaled with 'outer-flow'-scaling coordinates in figure 16(*b*) and appear to be consistent with the expected distribution shown in figure 4(*a*).

Let us now examine the behaviour of the high-wavenumber peel-off of the spectra from the $-\frac{5}{3}$-power-law distribution in figure 16(*a*). Earlier, we showed that the value at which the spectra peel off from the $-\frac{5}{3}$ power law owing to the effects of viscosity is expected to follow

$$k_1 z = \frac{M}{\kappa^{\frac{1}{4}}} (z_+)^{\frac{3}{4}}. \tag{33}$$

For u_1 spectra measured using a normal wire of length l the peel-off from the $-\frac{5}{3}$ law may be caused by the spatial-resolution limit of the probe rather than by the effects of viscosity. Such a peel-off is expected to follow

$$k_1 z \sim \frac{z}{l}, \tag{34}$$

because Wyngaard (1968) has shown that the highest wavenumber resolvable by a wire of length l is given by $k_1 = O(1/l)$.

Let $(k_1 z)_{\mathrm{p}}$ be the experimentally determined peel-off point. This point can be calculated using the method illustrated in figures 17(*a*, *b*). Figure 17(*c*) shows a plot of $\log (k_1 z)_{\mathrm{p}}$ versus $\log (z_+)$ determined from u_1 spectra measured at the same Reynolds number with wires of different length. Provided that z/l is sufficiently large the data appear to follow a line of slope $+\frac{3}{4}$. However, as z decreases the data appear to fall closer to the line of slope $+1$. It can be seen that, with the use of shorter wires, evidence for the peel-off following (33) becomes more substantial. By extrapolating the data in figure 17(*c*) to zero wire length, we obtain an estimate $M = 0.085$. When the data shown in figure 16(*a*) are scaled with Kolmogoroff coordinates the extent of the inertial subrange was greater for the spectra measured with the 0.39 mm wires than that measured with 1.26 mm wires. Thus spatial resolution is a problem whenever we are attempting to verify the existence of a Kolmogoroff region in laboratory-produced flows. PC in their interpretation of the data of Perry & Abell (1977) came to the conclusion that no Kolmogoroff region existed and that the spectra could be explained solely in terms of attached coherent motions.

Let us examine the behaviour of the spectrum at low wavenumbers. In figure 16(*a*, *b*) a small deviation above the inverse-power-law distribution is apparent at low wavenumbers in each spectrum. It was seen earlier that such deviations can be accounted for by the inclusion of a weighting function $W(\delta/\Delta_{\mathrm{E}})$. This deviation is more apparent in the pre-multiplied spectra scaled with 'outer-flow'-scaling coordinates as shown in figure 18(*a*). A simulation was carried out to determine what effect the inclusion of such a weighting function has on the predicted u_1 spectral distribution. For simplicity, this simulation used PC's spectral model, a discrete p.d.f. of hierarchy scales with a resolution factor r of 4, and the weighting function conjectured to be appropriate for a pipe is given in figure 9(*c*) with $a = d = 2.0$. Curve (i) in figure 18(*b*) shows the spectral prediction without the inclusion of the weighting function and curve (ii) that with the inclusion of the weighting function for a value z/Δ_{E} comparable with the values of z/Δ_{E} for the data shown in figure 18(*a*). A similar deviation at low wavenumbers is apparent in the streamwise spectral data of Perry & Abell (1975) in their figure 11(*a*), of figure 6(*a*) for $y_+ = 215$ of Bremhorst & Walker (1976), and of figure 11 for $y_+ = 200$ and 500 of Bullock, Cooper & Abernathy (1978). All of these spectra were measured in the turbulent wall region. Recently, a colleague

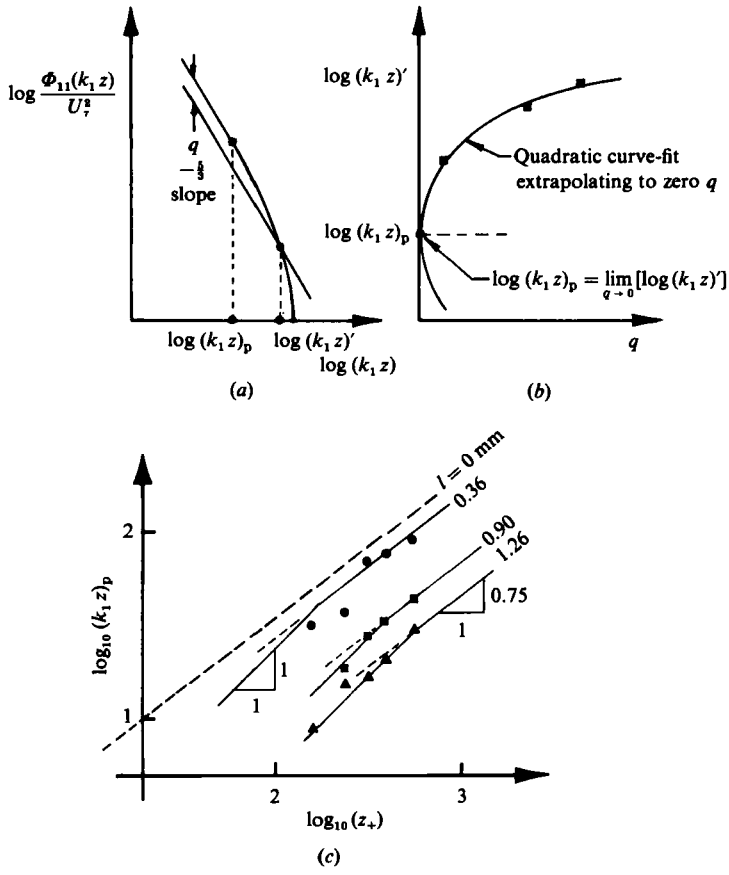

FIGURE 17. (*a*, *b*) The method used for determining $(k_1 z)_p$. (*c*) Values of $\log_{10}(k_1 z)_p$ versus $\log_{10}(z_+)$ obtained from u_1 spectra measured with normal wires of differing etched lengths l.

K. L. Lim (private communication, 1984) has obtained u_1 spectral data for flow over a smooth flat plate with a zero streamwise pressure gradient. A typical result is shown in figure 18(*c*) and it shows a similar deviation but with a value of a of about 3.5. Curve (iii) in figure 18(*b*) shows the predicted spectral result for $a = 3.5$. This value of a roughly corresponds to the value needed to obtain the Hama velocity-defect-law formulation using stretched Π-eddies (see §3.1).

The incomplete collapse of the data at low $k_1 \Delta_E$ in figure 16(*b*) may be due to the invalid use of Taylor's (1938) hypothesis, which utilizes one single convection velocity for all eddy scales at a fixed point in the flow. It is suspected that the larger-scale coherent attached eddies are convected downstream at a faster rate than the smaller-scale coherent eddies; hence there is a spread in convection velocities for a given wavenumber (e.g. see Wills 1964, who studied jets). A crude simulation was carried out to see whether this lack of collapse of the data could be explained by a spread in the convection velocity of the coherent attached eddies. The predicted u_1 spectral distribution from the model shown as curve (ii) in figure 18(*b*) is reproduced as the heavy curve in figure 19. This was calculated by Fourier-decomposing the *spatial* variation in velocity for each representative eddy or hierarchy (giving the wavenumber directly) and is therefore independent of the convection velocity of the eddies. This we will regard as the true spectrum. To

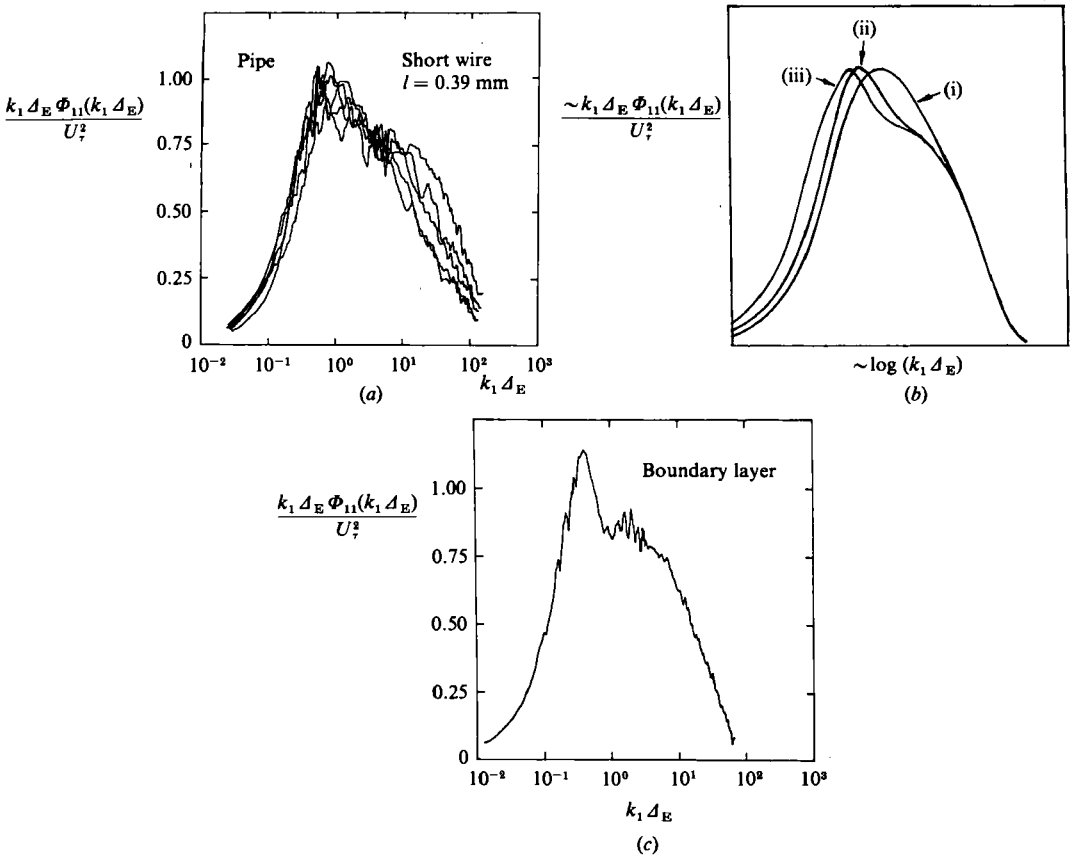

FIGURE 18. (*a*) Figure 16(*b*) presented as a pre-multiplied u_1 spectrum. (*b*) Computed pre-multiplied u_1 spectra using (i) no weighting function, (ii) weighting for a pipe and (iii) weighting function for a boundary layer ($a = 3.5$). (*c*) pre-multiplied u_1 spectra measured in a turbulent boundary layer, $z/\Delta_E = 0.0296$, $\overline{U_{1E}} \Delta_E / \nu = 130700$, Lim (1984).

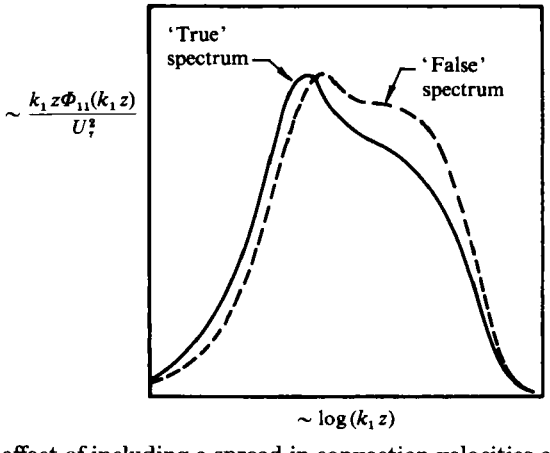

FIGURE 19. The effect of including a spread in convection velocities of the Λ-shaped eddies on the computed frequency spectrum which has been converted to wavenumber spectra using Taylor's (1938) hypothesis.

illustrate the effect of a spread in convection velocities of the eddies, this spectrum was recalculated as follows: it was assumed that the convection velocity for a hierarchy of scale δ is invariant with z and equal to the local mean velocity at $z = \frac{1}{2}\delta$ calculated using (3); the frequency spectrum as seen by a stationary probe at a distance z from the wall was then calculated and the argument of this spectrum converted from frequency to wavenumber using Taylor's hypothesis with a single convection velocity equal to the local mean velocity at z calculated using (3). The result is shown by the dotted line in figure 19. It can be seen that the low-wavenumber bump or deviation has been attenuated and the suggestion of another bump at high wavenumbers is apparent. This curve bears a strong resemblance to that of the data of Perry & Abell (1975) mentioned earlier. The low-wavenumber shift seen in figure 19 can be shown to vary with z/Δ_E and the variation, though not as large, is consistent with that of the data shown in figure 16 (*b*) and 18 (*a*). Hence the invalid use of Taylor's hypothesis has a measurable effect and prevents the data when plotted with outer-flow-scaling coordinates from collapsing at low wavenumbers.

(ii) u_3 spectra. The u_3 spectra measured in the turbulent wall region are shown in figure 20 with 'inner-flow'-scaling coordinates for varying values of z/Δ_E at six different Reynolds numbers. The data at low and moderate $k_1 z$ correlate reasonably with the expected distribution shown in figure 5 (*a*). More importantly, there is no inverse-power-law region and no systematic peel-off of the spectra at low $k_1 z$ as is characteristic for the u_1 spectra (see figure 16*a*). This fact alone lends strong support for the Townsend attached-eddy hypothesis and the model of PC. The slight spread in the u_3 spectra at low $k_1 z$ cannot be explained by a spread in convection velocity of the eddy scales, since a probe sensitive only to u_3 motions only 'sees' eddies of scale $\delta = O(z)$. The authors contend that this spread may be caused by cross-contamination of the X-wires from the u_2 motions. This will occur if the X-wires are rolled about the streamwise axis or if the hot-wire filaments are bowed. In figure 20 no inertial subrange is observed and the peel-offs at high $k_1 z$ depend upon z/Δ_E and not z_+; since the corresponding u_1 spectra (which were measured using normal wires) showed a distinct inertial subrange, we suspect that the spatial-resolution limit of the X-wires may dominate the form of the spectrum in this region. If this were the case, the data when scaled with 'outer-flow'-scaling coordinates should collapse at high $k_1 \Delta_E$, since for these experiments the X-wire geometry and scale was fixed. Hence the resolution limit of the probe happened to scale with Δ_E since l/Δ_E is fixed. This is confirmed in figure 21, where the data are presented with 'outer-flow'-scaling coordinates. The spread in the data at low $k_1 \Delta_E$ with z/Δ_E has increased significantly and this is in agreement with the spectral proposal shown in figure 6 (*a*).

4.2.2. *The fully turbulent region*

Here we will discuss the spectra which occur over the entire fully turbulent region, which extends from the outer limit of the buffer zone to the pipe centreline. According to the Townsend Reynolds-number-similarity hypothesis, the spectrum of the energy-containing components of the u_i velocity fluctuations in this region should follow

$$\frac{\Phi_{ii}(k_1 z)}{U_\tau^2} = q_i\left(k_1 z, \frac{z}{\Delta_E}\right), \tag{35}$$

where $i = 1$, 2 or 3 and q_i is independent of viscosity. At high wavenumbers a Kolmogoroff region should exist and provided that the Reynolds number of the flow is sufficiently large this should include an inertial subrange. Of course this region can only be derived from dimensional analysis and not from the attached-eddy model.

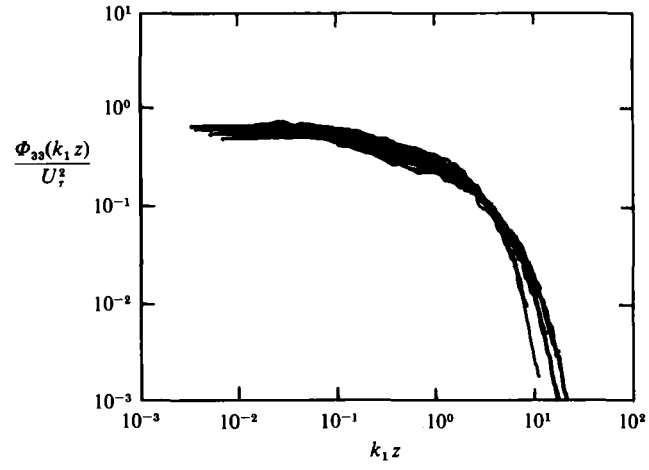

FIGURE 20. u_3 spectra scaled with 'inner-flow'-scaling coordinates for varying values of z/Δ_E within the turbulent wall region and for six Reynolds numbers equally spaced from 75000 to 200000.

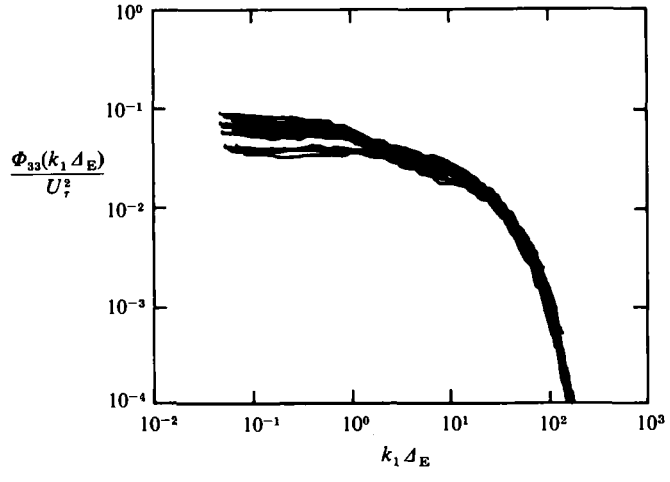

FIGURE 21. u_3 spectra shown in figure 20 scaled with 'outer-flow'-scaling coordinates.

(i) u_1 spectra. The u_1 spectra for six different Reynolds numbers, ranging from 75000 to 200000, are presented in figure 22(*a–f*). In each figure the wall distance varies from the pipe centreline ($z/\Delta_E = 1.0$) to a value of z/Δ_E close to the outer limit of the buffer zone. Figure 24(*a*) shows a superimposed selection of data from figure 22(*a–f*) and it is seen that (35) is applicable in the energy-containing region, at least for the range of Reynolds numbers examined here. At a fixed z/Δ_E, the slight spread in the spectra at low $k_1 z$ with Re is thought to be due to a change in the fractional spread of the convection velocities of the eddies as Re changes (see Perry & Abell 1977).

That part of the u_1 spectral results that can be described by (35) are similar to those predicted by PC, i.e. for the coherent attached eddies. Spectral distributions have also been computed using the method detailed in §3.2 for a Λ-vortex without the use of a weighting function. A Kolmogoroff region is not included in these calculations. These are shown in figure 25(*a*) for a range of values z/Δ_E. Even though these

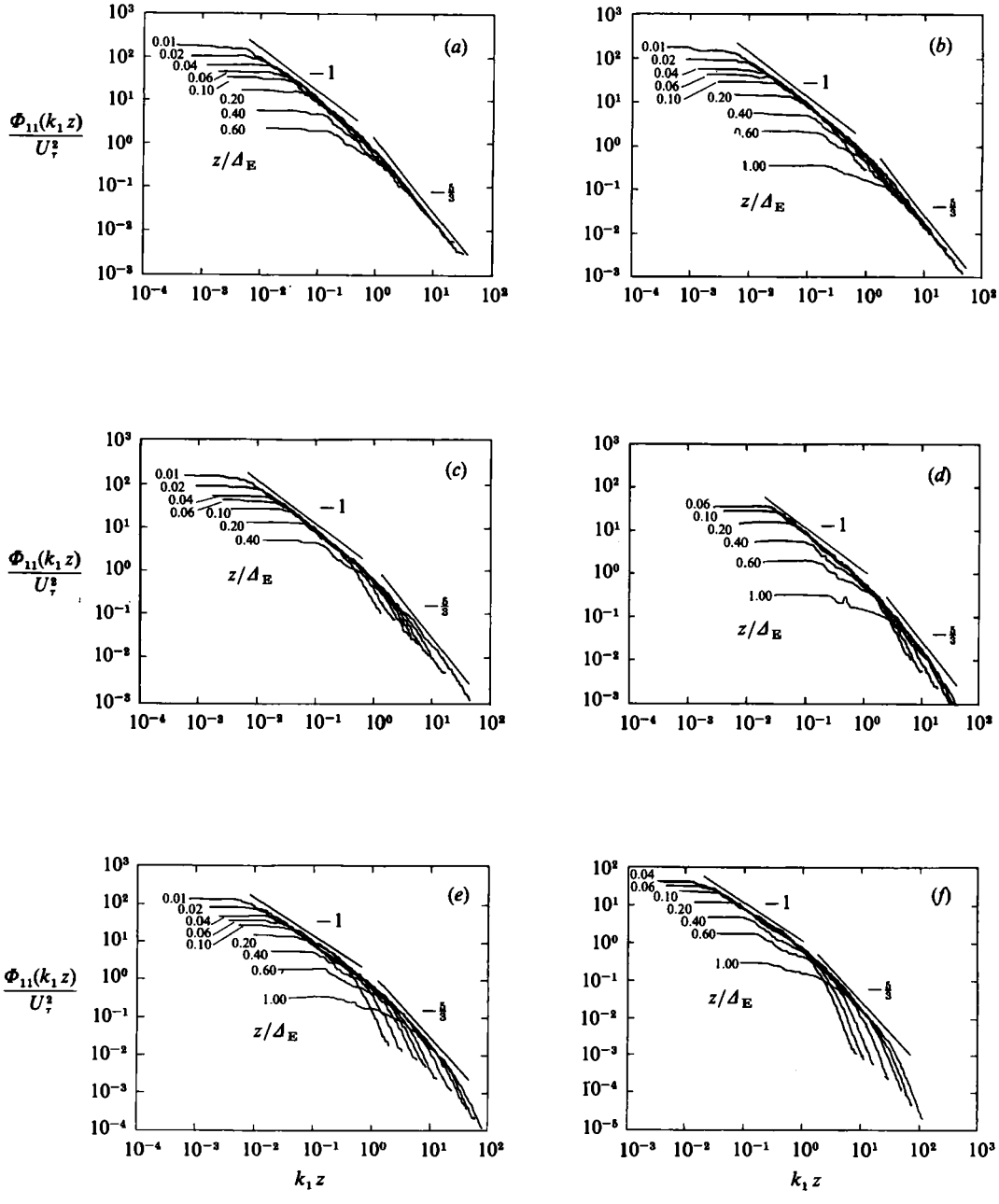

FIGURE 22. u_1 spectra spanning the whole turbulent region scaled with 'inner-flow'-scaling coordinates at six Reynolds numbers for varying values of z/Δ_E. (*a*) $Re = 200000$, $U_\tau = 1.188$ m/s; (*b*) 175000, 1.041; (*c*) 150000, 0.920; (*d*) 125000, 0.777; (*e*) 100000, 0.635; (*f*) 75000, 0.487.

calculations are applicable only to flow over a smooth flat surface as mentioned earlier, they show a distinct resemblance to the experimental pipe data shown in figure 22. It is remarkable how small a value of z/Δ_E is required before a substantial length of inverse-power-law region is apparent in the predicted u_1 spectra. This also seems to be so for the experimental spectra.

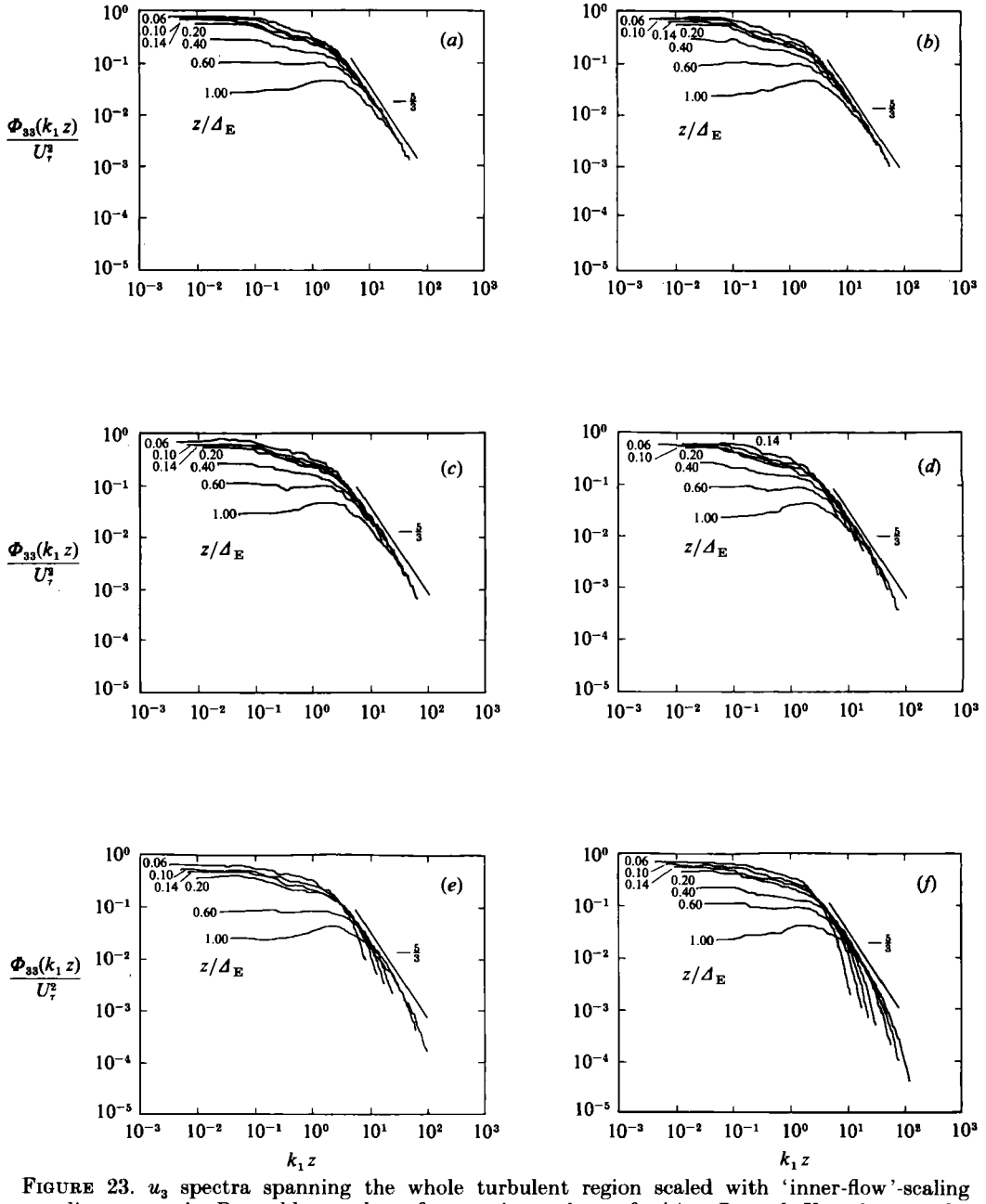

FIGURE 23. u_3 spectra spanning the whole turbulent region scaled with 'inner-flow'-scaling coordinates at six Reynolds numbers for varying values of z/Δ_E. *Re* and U_τ values as for figure 22.

Let us now return to figure 22. At the two highest Reynolds numbers, figure 22 (*a*, *b*), the data at high $k_1 z$ collapse to an inertial subrange. As the Reynolds number of the flow is decreased, the effect of viscosity becomes more important in this high-wavenumber region and the spectra peel off from the inertial subrange ($(-\frac{5}{3})$-power-law region) at decreasing values of $k_1 z$ as z/Δ_E increases for a fixed Reynolds number. This $-\frac{5}{3}$-power-law region evolves into a $-\frac{5}{3}$-power-law 'envelope' at the lower Reynolds numbers.

(ii) u_3 spectra. The corresponding u_3 spectra are presented in figures 23(*a–f*). At high $k_1 z$ the data behave in a manner similar to the corresponding part of the u_1 spectra. It can be seen that, for z sufficiently large, the spatial-resolution limit of the X-wires in the Kolmogoroff region is no longer a problem, since the dissipation ϵ is small and so η is large. Figure 24(*b*) is a superposition of the data shown in figure 23(*a–f*) and it appears that (35) is upheld for the energy-containing u_3 motions.

Figure 25(*b*) shows the u_3 spectra computed using the Λ-vortex model for various values of z/Δ_E. These computed spectra show that, for z/Δ_E sufficiently small, that part of the spectrum due to the coherent attached eddies is universal for all wavenumbers, as was shown in earlier sections.

A comparison of the computed u_1 and u_3 spectra with the corresponding experimental data in figure 24(*a*, *b*) give encouraging support for the existence of a range of scales of geometrically similar hierarchies, consisting of coherent attached eddies, as was proposed by PC for wall-shear flow.

4.3. *Broadband turbulence results*

4.3.1. *Turbulence results for* u_1

Distributions of $\overline{u_1^2}/U_\tau^2$ measured in the fully turbulent region are shown in figure 26 for various values of $\Delta_E U_\tau/\nu$. Also shown are the predicted distributions of $\overline{u_1^2}/U_\tau^2$ using (14) for the highest and lowest experimental values of $\Delta_E U_\tau/\nu$. These predictions are applicable only in the turbulent wall region and the values of A_1, B_1 and C have been estimated from the experimental spectra to be 0.90, 2.67 and 6.06 respectively. In the turbulent wall region there is a systematic variation of the data with $\Delta_E U_\tau/\nu$ at a fixed z/Δ_E that is significantly greater than the predicted variation. This variation of the data extends beyond the turbulent wall region and still exists, though to a lesser extent, at the pipe centreline. The authors conjecture that this variation may be due to the distortion of the geometry of the coherent attached eddies in the smallest hierarchy by the circular boundary condition of the pipe. We imagine that this distortion is transmitted to the eddies in the larger hierarchies, which are formed in stages from the smallest hierarchy by a vortex-pairing process. The 'degree' of distortion will depend upon the ratio of the smallest hierarchy scale (which scales with ν/U_τ) to the radius of curvature of the pipe. This ratio is proportional to $\Delta_E U_\tau/\nu$, the Kármán number. In the limit as $\Delta_E U_\tau/\nu \to \infty$, this influence should vanish and the Townsend Reynolds-number-similarity hypothesis should be upheld. This lack of Reynolds-number similarity, which is apparent even in the largest-scale eddies, is difficult to see in the experimental spectra because of the complicating effect of the spread in convection velocity of the eddy scales discussed earlier. Perry & Abell (1977) also observed a lack of Reynolds-number similarity even in the large scale motions and attributed this to an insufficient flow-development length in their pipe. In the present study the development length was approximately five times larger and the Reynolds-number effect is still present.

4.3.2. *Turbulence results for* u_3

Figure 27 shows the distributions of $\overline{u_3^2}/U_\tau^2$ measured in the fully turbulent region for various values of $\Delta_E U_\tau/\nu$. According to the analysis in §2, the distribution in the turbulent wall region should be given by (16). However, the effect of the viscous cutoff given by the second term in (16) is masked by an even stronger cutoff, namely the spatial-resolution limit of the X-wires, as was confirmed by the u_3 spectra measured

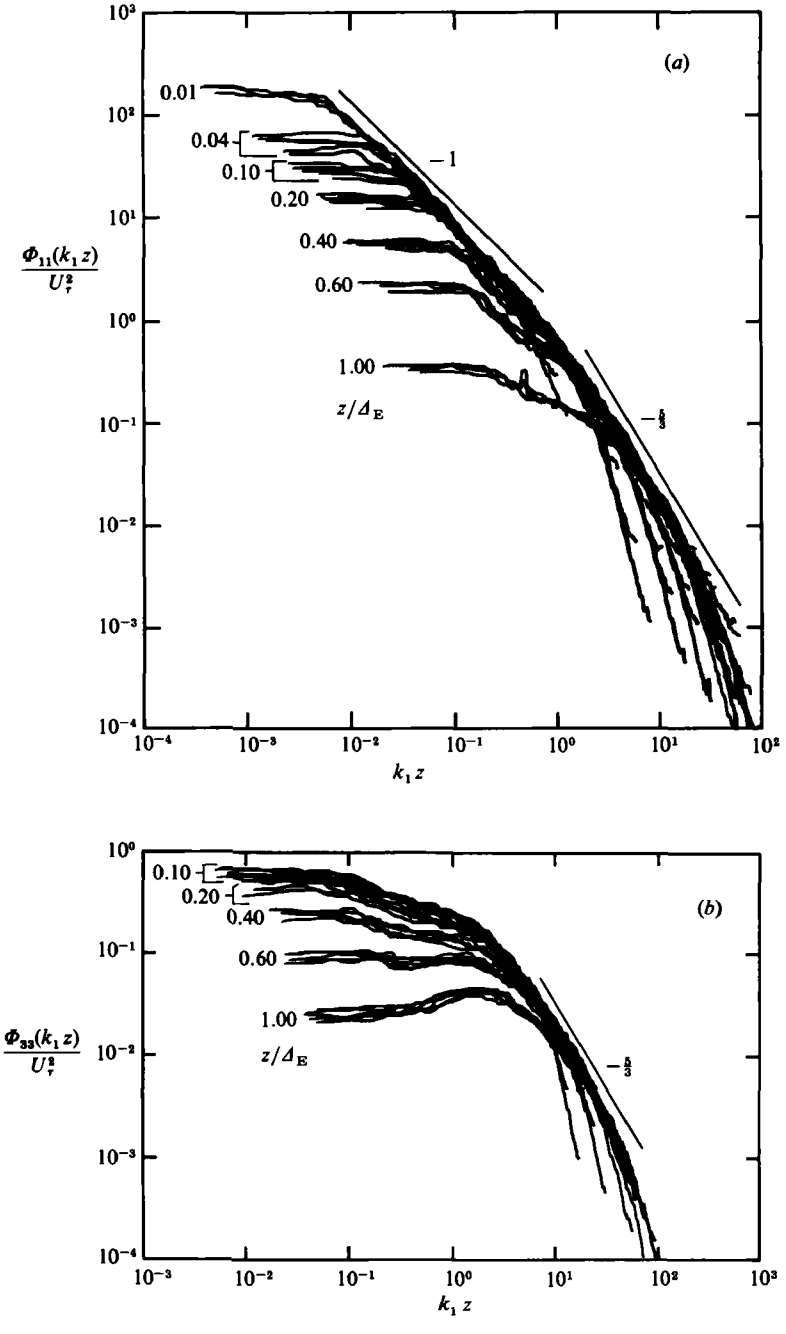

FIGURE 24. (*a*) A superposition of some of the u_1 spectral data shown in figure 22(*a–f*). (*b*) A superposition of the u_3 spectral data shown in figure 23*a–f*).

in the turbulent wall region (see figure 20). There is no systematic variation of these results with $\Delta_E U_\tau/\nu$. It was conjectured that the high-wavenumber cutoff of the u_3 spectra was controlled by the scale of the X-wires. This means that the broadband data should collapse with 'outer-flow' scaling, since l/Δ_E was held approximately constant.

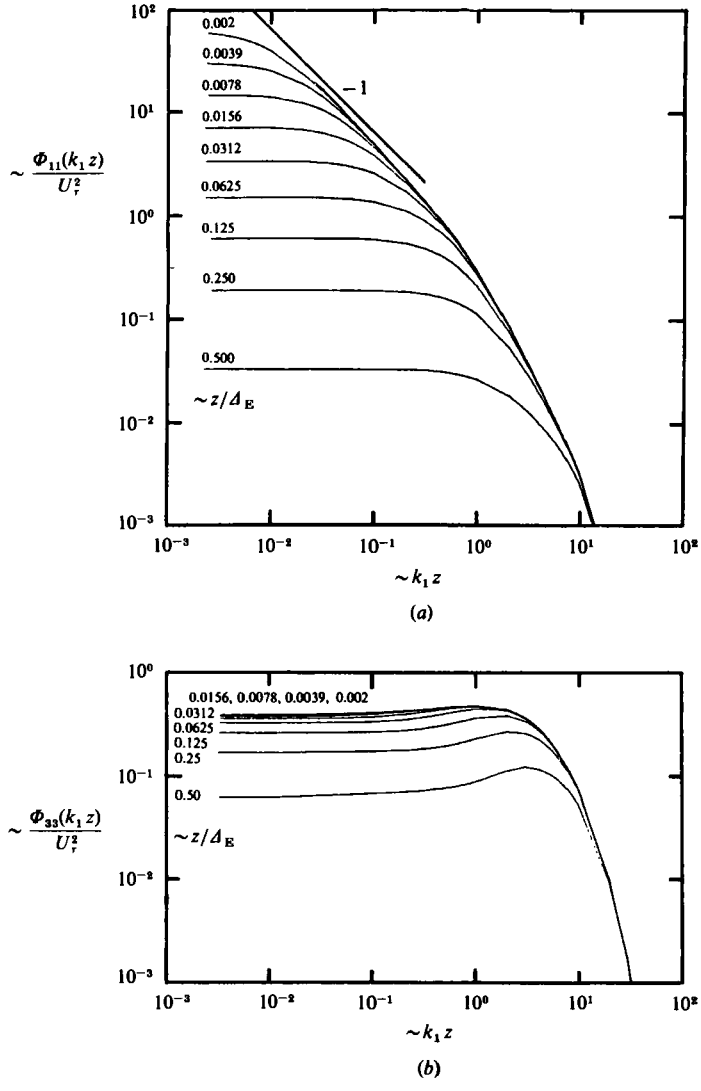

FIGURE 25. Spectra computed using the Λ-vortex model for varying values of z/Δ_E scaled with 'inner-flow'-scaling coordinates. (*a*) u_1 spectra. (*b*) u_3 spectra.

The fact that the data collapse to a region of constant $\overline{u_3^2}/U_\tau^2$ in the turbulent wall region is fortuitous and does not necessarily confirm the asymptotic prediction given by (16) and by (29*c*). Figure 28 shows the results of a crude simulation which used the eddy-intensity function $I_{33}(\lambda)$ shown in figure 15(*b*) and the weighting function used earlier for pipes. The low cutoff λ_1 shown in figure 15(*b*) was replaced by $\lambda_l = \ln(l/z)$ to simulate the spatial-resolution limit of the probe. Here, the value of λ_l was allowed to be greater than zero and hence had an effect on the integral. For $l = 2.00$ mm, a flat region is predicted for values of z/Δ_E comparable with those of the data shown in figure 27 for the turbulent wall region.

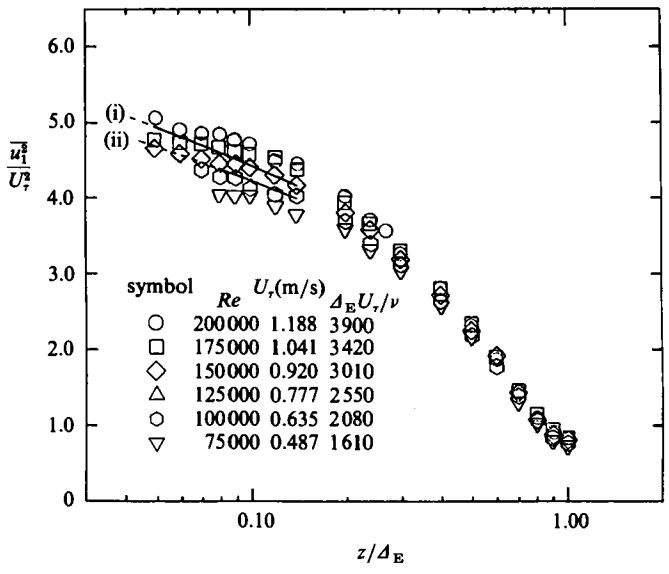

FIGURE 26. $\overline{u_1^2}/U_\tau^2$ distributions for varying values of $\Delta_E U_\tau/\nu$. Curves (i) and (ii) are the predicted distributions using equation (14) for the highest (3900) and lowest (1610) experimental values of $\Delta_E U_\tau/\nu$ respectively ($A_1 = 0.90$, $B_1 = 2.67$ and $C = 6.06$).

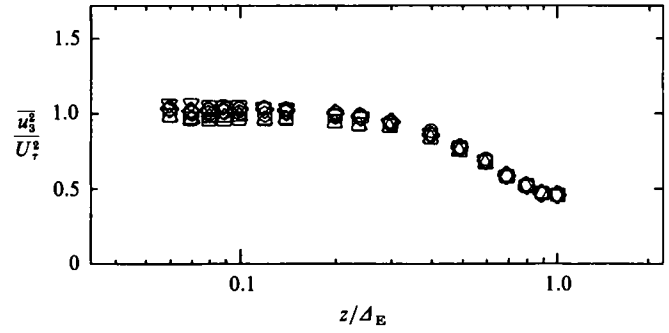

FIGURE 27. $\overline{u_3^2}/U_\tau^2$ distributions for varying values of $\Delta_E U_\tau/\nu$. Symbols as for figure 26.

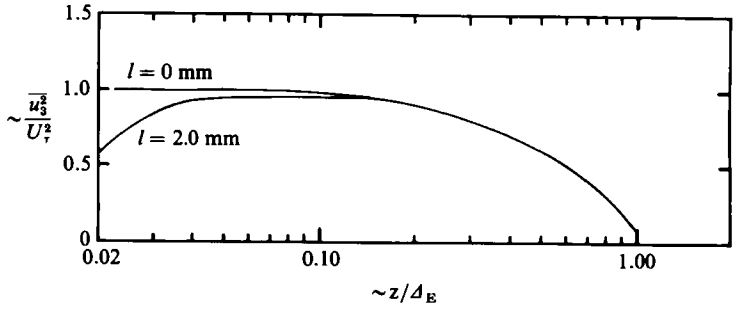

FIGURE 28. $\overline{u_3^2}/U_\tau^2$ distribution calculated using the Λ-vortex model and the weighting function for a pipe with a spatial-resolution cutoff determined by the effective X-wire lengthscale l. Here, $l = 0$ mm and 2.00 mm.

5. Conclusions

From their analysis and measurements, the authors propose the following picture of wall turbulence. Attached coherent eddies are formed from the viscous-sublayer material and have a lengthscale corresponding to the Kline scaling and a velocity scale equal to the wall-shear velocity. They stretch and grow with a fixed orientation relative to the wall and are said to belong to the 'first hierarchy' of eddy scales. They either die by viscous diffusion and vorticity cancellation or else pair or merge to produce eddies of a larger lengthscale, and these eddies are said to belong to the 'second hierarchy'. This process repeats itself, giving a range of scales of geometrically similar hierarchies. The p.d.f. of hierarchy lengthscales is assumed to be of inverse-power-law form and all hierarchies have the same characteristic velocity scale. These two assumptions lead to the logarithmic law of the wall, a region of constant Reynolds shear stress and an inverse-power-law spectral region for the fluctuating velocity components parallel to the wall in the turbulent wall region. These attached eddies are responsible for the mean vorticity, Reynolds shear stress and most of the energy-containing motions. It is conjectured that they do not contribute to the turbulent energy dissipation, except perhaps for the two smallest hierarchies. In §4.2.1 spectral data were presented which showed support for the above picture of wall turbulence and for the existence of a Kolmogoroff spectral region with an inertial subrange. It has been shown by Perry & Chong that attached eddies alone cannot explain the existence of a Kolmogoroff region. Here, we propose that the attached eddies are surrounded by detached isotropic fine-scale eddies which are responsible for a Kolmogoroff spectral region and for most of the turbulent energy dissipation. The authors suggest that these eddies originate from the debris of dead attached-eddy material which has been convected away from the wall and stretched and distorted by the larger-scale attached eddies. From this model of wall turbulence it appears that there is an energy flow to low wavenumber, due to eddy pairing, and an energy flow to high wavenumber in the Kolmogoroff region. No physical model, such as a cascade process, has been developed here and the existence of an inertial subrange has been explained only by the conventional dimensional-analysis argument.

The dimensional-analysis approach of Perry & Abell (1977) to wall turbulence has been extended to include all three components of velocity and the analytical deductions are consistent with the detailed physical model developed here, which was based on Townsend's (1976) attached-eddy hypothesis and the model of Perry & Chong (1982). The hypothesis of Townsend and the model of Perry & Chong were only applicable in the turbulent wall region and have been extended here to include the 'wake' region. This involved modifying the inverse-power-law p.d.f. proposed by Perry & Chong so that the model would give a mean-flow-velocity distribution that follows the Hama (1954) velocity-defect law and the low-wavenumber behaviour seen in experimental spectra of velocity components parallel to the wall (streamwise and lateral) measured in the turbulent wall region. This required a higher eddy population for the large-scale eddies and the type of modification to the hierarchy p.d.f. needed depends on the type of flow being considered (i.e. boundary-layer, pipe or duct flow).

Various eddy shapes and p.d.f.'s have been chosen in an attempt to correlate the analysis with the experimental data. No definitive eddy shape or p.d.f. has emerged and their exact form is still uncertain. Nevertheless, they lead to all the correct analytical expressions for the mean flow and spectra. Thus a link exists between the mean-flow distribution in the Coles 'wake' region and spectra of velocity fluctuations

parallel to the wall measured in the turbulent wall region. The broadband turbulence-intensity measurements are also consistent with the analysis but are less definitive in establishing the detailed structure of wall turbulence.

The link between the turbulence structure in the turbulent wall region and the outer-flow 'wake' region might possibly lead to a closure model in the prediction of a turbulent boundary layer in an adverse pressure gradient. Assuming that the hierarchy spectral function is unaffected by the presence of a pressure gradient, then a link exists between the Reynolds-shear-stress profile and the mean-velocity profile. The link is the p.d.f. of hierarchy lengthscales, which when coupled with the mean-flow momentum equation (Reynolds boundary-layer equation) might form the basis of a prediction scheme.

The authors wish to acknowledge the financial assistance of the Australian Research Grants Scheme.

REFERENCES

ACARLAR, M. S. & SMITH, C. R. 1984 An experimental study of hairpin-type vortices as a potential flow structure of turbulent boundary layers. *Rep.* FM-5. Dept of ME/Mech., Lehigh University.

BATCHELOR, G. K. 1956 *Theory of Homogeneous Turbulence.* Cambridge University Press.

BREMHORST, K. & WALKER, T. B. 1973 Spectral measurements of turbulent momentum transfer in fully developed pipe flow. *J. Fluid Mech.* **61**, 173–186.

BULLOCK, K. J., COOPER, R. E. & ABERNATHY, F. H. 1978 Structural similarity in radial correlations and spectra of longitudinal fluctuations in pipe flow. *J. Fluid Mech.* **88**, 585–608.

COLES, D. E. 1956 The law of the wake in the turbulent boundary layer. *J. Fluid Mech.* **1**, 191–226.

HAMA, F. R. 1954 Boundary layer characteristics for smooth and rough surfaces. *Trans. Soc. Naval Arch. Mar. Engrs* **62**, 333–358.

HEAD, M. R. & BANDYOPADHYAY, P. 1981 New aspects of turbulent structure. *J. Fluid Mech.* **107**, 297–337.

HUSSAIN, A. K. M. F. 1982 Coherent structures – reality or myth. *Rep.* FM-17. Dept. of Mech. Eng., University of Houston.

ISAKSON, A. 1937 On the formula for the velocity distribution near walls. *Tech. Phys. U.S.S.R.* **IV**, 155.

KIM, J. 1985 Evolution of a vortical structure associated with the bursting event in a channel flow. *Fifth Symp. on Turbulent Shear Flows, Cornell University, Ithaca, New York, 9.23.*

KLINE, S. J., REYNOLDS, W. C., SCHRAUB, F. A. & RUNDSTADLER, P. W. 1967 The structure of turbulent boundary layers. *J. Fluid Mech.* **30**, 741–773.

KOLMOGOROFF, A. N. 1941 The local structure of turbulence in incompressible viscous fluid for very large Reynolds numbers. *C.R. Acad. Sci. U.R.S.S.*, **30**, 301–305.

MILLIKAN, C. D. 1939 A critical discussion of turbulent flows in channels and circular tubes. In *Proc. 5th Congress of Appl. Mech. Cambridge, Mass.* (ed. J. P. Dentlartog & H. Peters), pp. 386–392. Wiley.

MOIN, P. & KIM, J. 1985 The structure of the vorticity field in turbulent channel flow. Part 1. Analysis of instantaneous fields and statistical correlators. *J. Fluid Mech.* **155**, 441–464.

PERRY, A. E. 1982 *Hot-Wire Anemometry.* Clarendon.

PERRY, A. E. & ABELL, C. J. 1975 Scaling law for pipe flow turbulence. *J. Fluid Mech.* **67**, 257–271.

PERRY, A. E. & ABELL, C. J. 1977 Asymptotic similarity of turbulence structures in smooth- and rough-walled pipes. *J. Fluid Mech.* **79**, 785–799.

PERRY, A. E. & CHONG, M. S. 1982 On the mechanism of wall turbulence. *J. Fluid Mech.* **119**, 173–217.

PERRY, A. E. & MORRISON, G. L. 1971 A study of the constant temperature hot-wire anemometer. *J. Fluid Mech.* **47**, 577–599.

SMITH, C. R. 1984 A synthesized model of near wall behaviour in turbulent boundary layers. In *Proc. of 8th Symp. on Turbulence, Dept. of Chem. Eng., University of Missouri-Rolla.*

TAYLOR, G. I. 1938 The spectrum of turbulence. *Proc. R. Soc. Lond.* A**164**, 476–490.

TOWNSEND, A. A. 1961 Equilibrium layers and wall turbulence. *J. Fluid Mech.* **11**, 97–120.

TOWNSEND, A. A. 1976 *The Structure of Turbulent Shear Flow* (2nd ed.). Cambridge University Press.

WILLS, J. A. B. 1964 On convection velocities in turbulent shear flow. *J. Fluid Mech.* **20**, 417–432.

ZAMAN, K. B. M. Q. & HUSSAIN, A. K. M. F. 1981 Taylor hypothesis and large-scale coherent structures. *J. Fluid Mech.* **112**, 379–396.